AN EXPERIMENTAL STUDY OF CONTROLLED GAS PHASE SYNTHESIS OF NANOSIZE TiO_2 POWDERS

by

Stephen D. LePera

Thesis submitted to the Faculty of the

Virginia Polytechnic Institute and State University

in partial fulfillment of the requirements for the degree of

MASTER OF SCIENCE

in

Mechanical Engineering

APPROVED:

U. Vandsburger, Chairman

L. A. Roe

R. J. Roby

October, 1994

Blacksburg, VA

2

An Experimental Study of Controlled Gas Phase Synthesis of Nanosize TiO_2 Powders

by
Stephen D. LePera
Committee Chairman: Uri Vandsburger
Virginia Polytechnic Institute and State University
Department of Mechanical Engineering

Abstract

Recently there has been an increased interest in the generation of ceramic powders composed of nanosize particles with a narrow size-distribution and high purity. It has been shown that ceramics sintered from these ultrafine particles exhibit improved mechanical and electrical properties. The present research has attempted to control the growth of the ceramic particles in a relatively simple continuous flow process by placing charges on the forming particles and controlling their evolution with an electric field.

Nanosize TiO_2 powder was produced using a multi-stream, co-annular reactor. The heat source was a cylindrical H_2/O_2 diffusion flame located around the outside of reaction zone. The effect on the powder size, shape, and size distribution due to particle charging, applied electric fields, and varying reactant concentrations were investigated.

The temperature field within the reaction zone was uniform radially and ramped axially from 600 to 1100 K. The reactant stream passed through a 10 millicurie Po-210 alpha source within the burner with the intention of creating a bipolar ion concentration. In the presence of an electric field, this ionization can lead to either a unipolar-negative or unipolar-positive particle charging environment. The electric field across the reaction zone was varied in an attempt to control particle residence time.

A rapid insertion cold-finger probe was built to extract samples from the reaction zone. This probe could be lowered rapidly through a glass tube into the reaction zone where the tip was briefly exposed to the local reactants and products. The particles stuck to the cooler surface of the probe until they were shaken off onto an electron microscope grid. This method of sample collection proved reliable, but lacked the desired spatial resolution and in many experimental conditions appeared to interfere significantly with the flow in the reaction zone.

Particles analyzed under a Tunneling Electron Microscope (TEM) were found to have average diameters of between 20 and 50 nm, depending proportionally on the concentration of the reactants.

The alpha source charger used was found to be ineffective at unipolar charging the forming ceramic particles. However, particles within the reactor appeared to naturally carry a negative charge.

The effectiveness of using an electric field to control the particle size distribution was inconclusive. Macroscopic observations showed a significant change in the reaction zone under different electric field configurations, but sampled particles were the same size from all comparable electric field conditions.

Acknowledgments

I would like to express my deep appreciation for the love and support my parents have given me throughout my life. Their support helps make all obstacles appear small. Without them it is unlikely I would have accepted the challenge of advanced education.

I would like to thank all the departmental faculty and staff who have assisted me in this work. It is difficult to realize without experience how important the departmental resources are to everyday experimental research. Most of the staff understand that this experience is educational, not just business, and have taught me as much as the faculty.

Special thanks are due to my committee members who have endured these times alongside me. I have been lucky to have three such sharp and helpful people to work with on this research.

Finally, I want to thank all the students that have worked with me in the Reacting Flows Lab and throughout the department for their assistance and friendship. It is easy to work on your own research, but it shows true friendship and support to help others. Thank you all.

Table of Contents

List of Figures

List of Tables

1 Introduction

1.1 Background and Motivation

Ceramics have high strength in compression, high temperature durability, and high wear resistance, but have been excluded over the years from applications where they may encounter high tensile stress loads. A small scratch or flaw weakens the tensile strength of a ceramic part so enormously that these parts will fail catastrophically under tension or bending. The brittleness of ceramic parts also means that they cannot, in general, be easily machined or shaped by the deformation processes used on metals without fear of cracking. The material has no ductility which would slow or stop propagation of cracks through metals like steel. The final properties of a ceramic material will clearly be dependent on its overall chemical composition but are also controlled by the size, shape, and purity of the elementary powder from which a part is fabricated.

Ceramic parts are made from a fine powder, usually held together with a binder. For instance, pottery is composed of clay, small aluminum silicate particles, and the water serves as a binder. The powder-binder composition is formed into the desired shape or pressed into a mold, and then the part is heated until the individual particles bond to one another through solid state diffusion of the atoms into the "pores" between particles. This densification process is called sintering. The original powder particles are now grains in the microstructure of the ceramic material. Grain growth, "pores" trapped within grains, and grain size are all very important to the final properties of a ceramic material (Shackelford, 1988).

Recently, there has been an increased interest in the generation of ceramic powders composed of nanosize particles with a narrow size distribution and high purity. Nanosize powders usually consist of particles less than 50 nanometers (50×10^{-9} m) in

diameter. Ceramics sintered from these ultrafine particles have been shown to exhibit improved mechanical and electrical properties (for instance, Brown, 1990). Their increased ductility and higher capacitance for equal physical dimensions make them attractive for use in micro-electronics as well as mechanical parts.

Many processes for the production of ultrafine powders have been proposed in materials research literature. These have been generally classified by Johnson (1987) as solution, salt decomposition, and vapor phase methods. With the exception of a method known as spray based particle separation, all solution techniques constitute batch processes where a batch of particles is prepared, usually using wet chemistry to precipitate out the solid phase particles. In order to make more particles, the chemical process is repeated. This is a disadvantage in industrial production where continuous processes are preferred. Salt decomposition methods involve reactions in the solid phase, followed by processing. Due to the nature of the reactants this is also a batch process. Vapor phase techniques involve the use of gaseous (vapor) phase reactions that result in the nucleation of a ceramic powder from the gas phase as shown in Figure 1. An advantage of vapor phase synthesis is that the reactants can be brought together to form solid particles in a continuous process, suited for industrial scale production. Nucleation, surface growth, and coagulation occur simultaneously as the particles develop. The difficulty, however, with vapor phase powder synthesis lies in achieving control over these rapid processes which determine the evolution of the particle size and size distribution. This was a prime motivation for the present study.

1.2 Literature Review

Literature in the field of ceramic powder formation as well as soot formation, aerosol dynamics, and optical diagnostics in combustion systems was reviewed to gain an

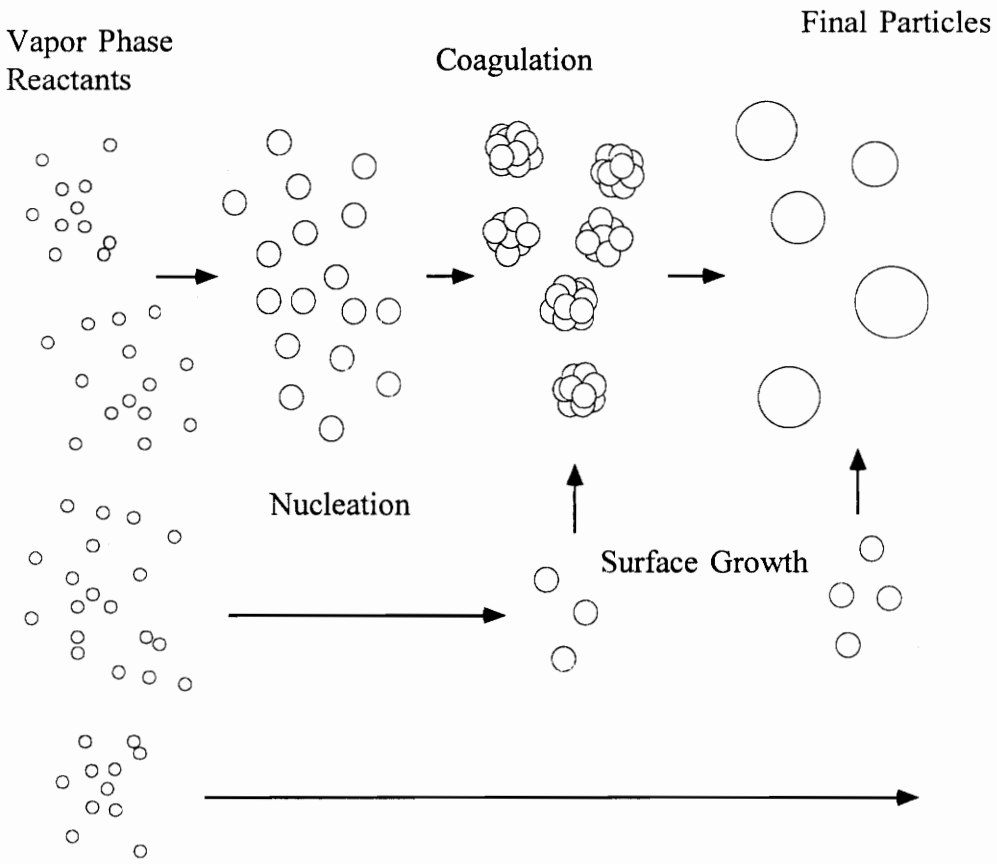

Figure 1. Nucleation, surface growth, and coagulation in the vapor phase formation of a ceramic powder.

understanding of the concepts involved. The following is a summary and, where sensible, a brief discussion of the papers and texts that most influenced and supported this work.

1.2.1 Overviews

An article in *Aerospace America* by Brown (1990) describes, in simplified terms, the anticipated benefits of producing nanosize ceramic powders with a narrow size distribution as increased ductility (claimed higher than 200%) and lowered sintering temperatures by over 300°K. From this and overviews such as Johnson (1987) and Flagan (1988) it can be generally accepted that the production of unagglomerated nanosize powders with a narrow size distribution is an important research objective. These sources give typical production rates of powder at 2 to 20 grams/day in batch processes, also lending support to the conclusion that nanosize powders should be produced in a continuous flow process. This is necessary if they are to become a viable commercial product.

1.2.2 Particle Charging in Electric Fields

The work found in Hardesty & Weinberg (1972) claimed that soot particle formation, size, and concentration could be modified by the application of electric fields. Also, in experiments with SiO_2, the particle size was reduced by as much as a factor of 3, due to the reduced residence time of the forming particles. The application of these findings to the production of ceramic powders suggests that attaching a charge to forming particles will allow control over the residence time, and thus the growth rate and final size of the forming powders. Hardesty & Weinberg (1972) described the mechanisms of particle charging as diffusion charging (where the attachment of charges to a particle are

along electric field lines), and thermionic charging (where the charging rate is highly dependent on the chemical and thermal characteristics of the flame). A more detailed discussion of these phenomena can be found in Lawton & Weinberg (1969). Simple calculations were performed based the correlations given by Hardesty & Weinberg (1972) and theoretical considerations from Hidy & Brock (1970). Because thermionic emission in flames is caused mostly by the combustion of hydrocarbons, thermionic charging was not expected to play a significant role in the present study due to the use of hydrogen as a fuel. The rate of charge acquisition by a single particle through the diffusion mechanism was given by Hardesty and Weinberg (1972) as

$$\left.\frac{dN}{dt}\right)_{\text{diff}} = \pi r_p^2 n_i \bar{c}_i \exp(-Ne^2 / r_p kT)$$

where r_p is the particle radius, n_i is the unipolar ion cloud number density, c_i is the ion mean thermal speed, e is the unit electrical charge, k is Boltzmann's constant, and T is temperature. The rate of charge acquisition by bombardment charging was given as

$$\left.\frac{dN}{dt}\right)_{\text{bomb}} = 3\pi r_p^2 n_i k_i E[1-(Ne/3Er_p^2)]$$

where E is the electric field strength and k_i is the ion mobility. From Hidy & Brock (1970) the effect of these attached electrostatic charges on the normal collision frequency is given, in the continuum regime, by the coefficient

$$\Omega_{ij}^c = \frac{z_i z_j e^2}{R_{ij} kT[\exp(z_i z_j e^2 / R_{ij} kT) - 1]}$$

where R_{ij} is the collision radius between two particles i and j, and z is the number of unit electrical charges carried by particle i or j. The results of these relations are given in Table 1 and Table 2 and can be seen to demonstrate the useful effect of particle charging. Because the Knudsen number for these diameters and concentrations places these particles between the free molecular and the continuum regimes, Ω_{FM} and Ω_C are both shown in the table. Even though charging time is inversely proportional to the square of the particle diameter, it was seen that a 10 nm particle in a field of unipolar ions could quickly acquire a charge and thus cause up to a 30-40% reduction in coagulation rate.

Table 1. Kinetic theory collision modification with Unipolar Charging , T=1500°K, and N=1 x 10^{16} $1/m^3$.

Particle Radius (nm)	Charge per Particle		Coagulation rate coefficient	
r	z_i	z_j	Ω_{FM}	Ω_C
5	1	1	.328	.544
5	1	2	.108	.269
5	2	2	.012	.052
10	1	1	.579	.747
10	2	2	.328	.544
10	2	2	.108	.269

Table 2. Particle Charging Times (seconds), n_i=1x10^{16}, ion is H_3O^+, E=3kV/cm

Particle	Charging Mechanism			
Radius	Diffusion		Bombardment	
(nm)	$t_{1\ charge}$	$t_{2\ charges}$	$t_{1\ charge}$	$t_{2\ charges}$
5	.013	.028	.0007	.0013
10	.0003	.0007	.00017	.00033
15	.00016	.00031	7.48 x 10^{-5}	.00015
20	8.7 x 10^{-5}	.00018	4.21 x 10^{-5}	8.42 x 10^{-5}

The work of Adachi, Romay, & Pui (1992) suggests a way of unipolar charging particles both positively and negatively. Their charger makes use of a Po-210 radioactive isotope to ionize gas molecules, producing bipolar ions within the range (about 6 cm) of the alpha particles. These ions are then separated by an electric field applied between two screens, leaving only positive or negative ions in the flow depending on the polarity of the field. The charger was able to place a unit charge on over 75% of the 10 nm diameter particles tested and 95% of particles with a 20 nm diameter. The charging efficiency was dependent on the flow rate through the reactor and the applied voltage across the charging zone. Higher flow rates reduced the percentage of particles that acquired a charge, while increasing the voltage increased the charge acquisition. However, increasing the voltage above a certain level resulted in increasing particle losses to the walls and the downstream electrode screen, implying that for a given design there are optimal flow rates and electric field strengths which will give the best particle charging.

1.2.3 Modeling of Aerosol Dynamics

The work of Pratsinis, Landgrebe, & Mastrangelo (1989) uses a method called discrete sectional modeling to predict the evolution of a powder size distribution. This model defines the rate of change of given size particles as a function of the rate of new particles appearance (nucleation) and the rate of coagulation, or collision, between existing particles as:

$$\frac{dn_i}{dt} = I(i^*)\delta(i-i^*) + \tfrac{1}{2}\sum_{j=1}^{i-1}\beta_{j,i-j}n_j n_{i-j} - n_i\sum_{j=1}^{i-1}\beta_{i,j}n_j$$

where n_i is the number of particles containing i molecules of the product (the number of particles of a given size). The first term on the right hand side gives the nucleation rate I

of particles of critical size i^*, while the last two terms give consecutively the gain and loss of n_i by coagulation. This equation was written in terms of dimensionless groups relating rates of coagulation and nucleation to each other. Dimensionless reaction time and dimensionless residence time help show the effect of each variable on the final size distribution. According to the model, the final average diameter of the powder distribution loses its dependency on reaction rate as the rate grows faster, i.e. if the reaction rate is very fast, then the final diameter depends solely on residence time. This method gives informative and qualitatively good results. However, in order to make their theory agree well with experimental data, they had to multiply the collision frequency by a factor of 2.2. Pratsinis *et al* (1989) believe this may be due to van der Waals forces, but part of the possible explanation for deviation may lie in the missing surface growth contribution. These might act like the collision terms if only transport rates were considered but would add mass to the system without increasing the number density.

1.2.4 Chemical Kinetics

Pratsinis, Bai, Biswas, Frenklach, & Mastrangelo (1990) studied the kinetics of the reaction between $TiCl_4$ and O_2 in a furnace flow reactor. Often, when a reaction is complicated, a correlation will be found to describe the overall (global) reaction rate so that the conversion from reactant to product can be calculated easily for appropriate concentrations and temperatures. This is the course of action taken by Pratsinis *et al* (1990).

Greater than 96% of the reaction took place in the isothermal zone of the reactor/furnace. The overall reaction for the conversion of $TiCl_4$ to TiO_2,

$$TiCl_4 + O_2 \rightarrow TiO_2 + 2Cl_2$$

was measured at temperatures between 700° and 1000°C, residence times between 0.27 and 1.27 seconds, and $TiCl_4$:O_2 concentrations from 1:1 to 1:40. The procedure followed by Pratsinis *et al* (1990) was to assume that there is a limiting reaction step involving the breakdown of $TiCl_4$ and that that step can be described with a first order Arrhenius reaction rate. The Arrhenius form can be written as a function of the reactant's original concentration, final concentration, the reaction time, and the temperature as shown. With $k = Ae^{-\frac{E}{RT}}$ where E is the activation energy and R is the gas constant, the rate of disappearance of $TiCl_4$ is

$$-\frac{d[TiCl_4]}{dt} = k[TiCl_4] \qquad \text{or}$$

$$-\frac{1}{[TiCl_4]}\frac{d[TiCl_4]}{dt} = k.$$

After integration between the reactant concentration in (i) and out (o), this becomes

$$\ln[TiCl_4]_o - \ln[TiCl_4]_i = k \cdot t$$

and is finally written as

$$\ln\left(-\frac{\ln\left(\frac{[TiCl_4]_o}{[TiCl_4]_i}\right)}{t}\right) = \ln A - \frac{E}{RT}.$$

The data was plotted and shown to lie on a line whose slope is correlated with the activation energy and whose intercept is the log of the preexponential factor. The result is a global rate of reaction proposed as

$$-\frac{d[TiCl_4]}{dt} = \left(k + k'[O_2]^{1/2}\right)[TiCl_4]$$

where

k=8.26 x 10^4exp(-E_a/RT) s^{-1}

k'=1.4 x 10^5exp(-E_a/RT) $(L/mol)^{1/2}$ s^{-1}

and

E_a=88.8±3.2 kJ/mol.

The extra dependence on the oxygen concentration comes from an observed experimental effect seen with high oxygen concentrations. This work shows the extreme importance of temperature distribution on the powder formation process. Between 300 K and 400 K there is an increase in reaction rate by four orders of magnitude. In Pratsinis' model this indicates a large number of nucleations, widening the size distribution as well as raising the number density and thus increasing the probability of collisions.

1.2.5 Ceramic Powder Generation

The value of the above kinetic data is easily seen in the results of Wu, Nguyen, & Flagan (1987). The authors used an electrically heated flow reactor to generate high purity, spherical, non-agglomerated particles in the 0.1 μm range. Their reactor had five discrete reaction zones, each at an increasing temperature. The nucleation rate in the lower temperature area was slow, leading to the formation of a low concentration of new, very small particles. Reactions continued in a gradually increasing temperature field, promoting the surface growth of these nuclei. As the particles grew they more easily scavenged reactants, suppressing new nucleations and allowing the temperature to be raised higher. The result was a small size distribution and, due to keeping the number density small, relatively low agglomeration. A disadvantage of this method was that the walls of the reactor serve as a site for heterogeneous nucleation.

Zachariah, Chin, Semerjian, & Katz (1989) used a counter flow H_2/O_2 diffusion flame to study the formation of ceramic powders, specifically the effect of reactant concentration, temperature, and flame equivalence ratio, noting that particle diameters were larger in cooler flames than in hotter flames. They explained that the reaction rate kinetics were very fast in the hotter flames, increasing the homogeneous nucleation rate and leading to the formation of large numbers of small particles, as expected from the above theory and chemical kinetic analysis. They also noted that higher temperatures tended to produce more spherical particles due to sintering effects. Cool flames showed significant surface growth, contributing to the production of larger particles. Larger reactant concentrations were seen to cause early particle inception as well as larger final diameters.

Katz & Hung (1990) reported a significant increase in particle size when an electric field was applied across the reaction zone. Their observations of particle motion within the reactor implied that the particles were being positively charged. Curiously, the application of the electric field caused a decrease in the residence time of the particles, but particle diameters grew by as much as a factor of ten. This is counter-intuitive, and no explanation was given to explain how the applied voltage might be responsible for the increased growth rate. Changing the polarity of the field had a negligible effect on the particle size and number density even though observations indicated that particles were following significantly different paths through the reaction zone (although all measurements were made along the stagnation line).

1.3 Proposed Work - Goals

This literature review led to the conclusion that production of particles in a wall free reactor would be an improvement over existing methods. In an effort to minimize

agglomeration and narrow the size distribution, the forming particles would be unipolar charged and subject to an electric field placed across the reaction zone. The particle residence time, and therefore surface growth, would be controlled by adjusting the electric field strength. The temperature field would be used to control the gas phase chemical kinetics and nucleation. The particle growth would be studied by collecting samples from the reactor and possibly monitoring the aerosol *in-situ* with optical diagnostics.

2 Experimental Setup and Procedure

2.1 Methodology

In the present work, particle synthesis took place in a flame based, surface free reactor using $TiCl_4$ as a reactant to form the titania powder TiO_2. Heterogeneous nucleation of the reactants was prevented by replacing the traditional electric heating of an outer wall with a co-annular diffusion flame. Variations in flow rate, temperature distribution, particle charging and electric fields were used in the attempt to effect the concurrent and rapid processes that control the final particle size distribution: nucleation, surface growth, and coagulation. Experiments were conducted and particles were removed from the reactor using a rapid insertion probe technique for analysis by a Tunneling Electron Microscope (TEM). A system was also set up to monitor particle size characteristics *in-situ* by using light scattering and absorption measurements.

A temperature distribution in the reactor that ramped from low temperatures (thus low reaction rate) to higher temperatures was used to control the competing rates of nucleation and surface growth. Calculations which showed that coagulation rates would be reduced due to coulombic repulsion for unipolar particle charging suggested it might be useful to generate particles in a bipolar, unipolar-negative, or unipolar-positive environment so that charges could attach to the particles while they formed. Residence time of the growing particles, an important variable in determining the final size of a particle, was to be controlled by adjusting the strength of an electric field across the reaction zone.

The following sections contain a description of the experimental apparatus and the procedures used in this work. An integrated schematic of the powder generation system is given in Figure 2.

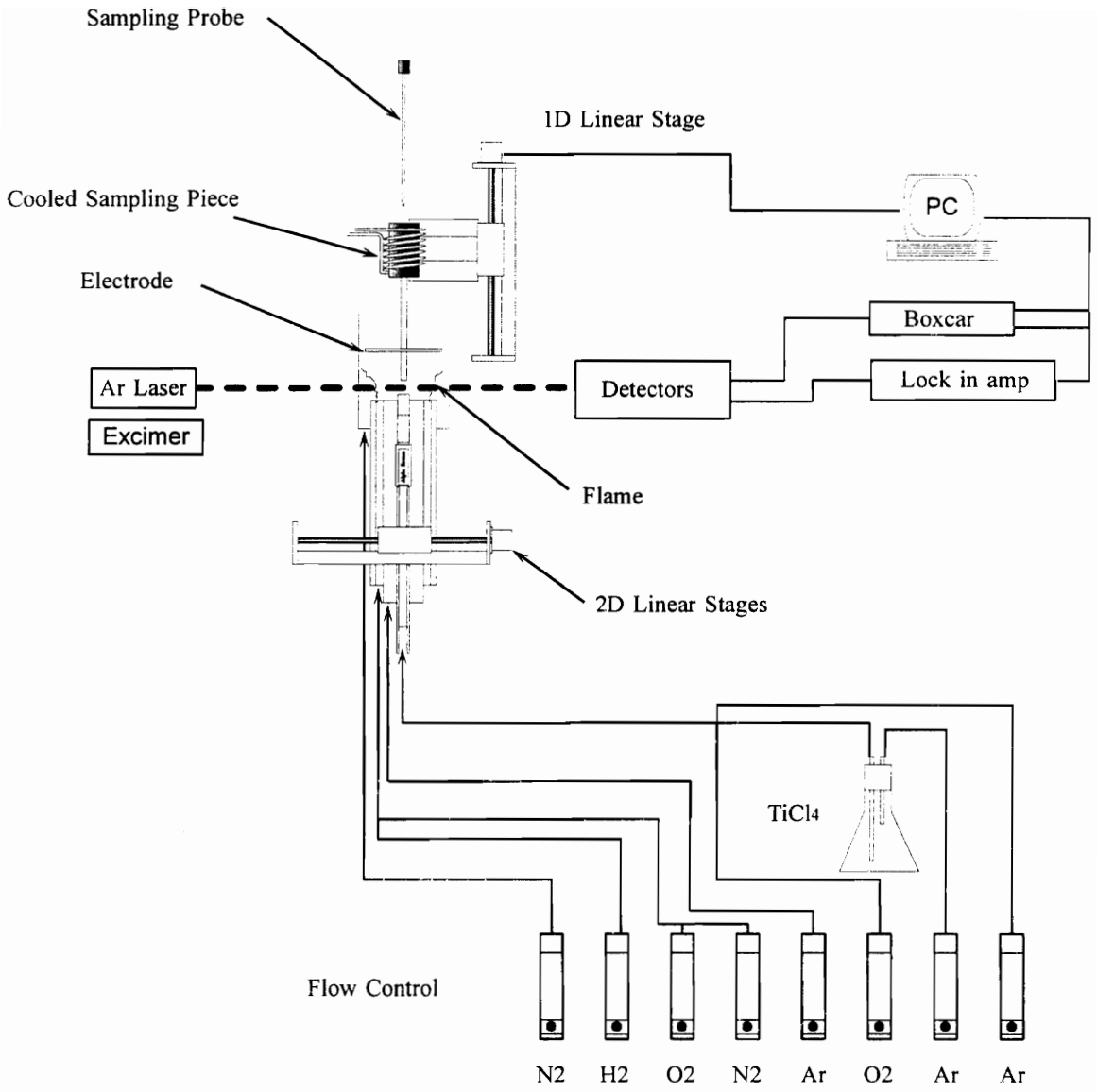

Figure 2. Schematic of powder generation system.

2.2 The Reactants

Titanium tetrachloride ($TiCl_4$), a high-vapor-pressure liquid at room temperature, was used as the reactant in this work because it is relatively simple to use in the vapor phase. Titania (TiO_2), the ceramic powder that results from the reaction of $TiCl_4$ and O_2, has been generated in the vapor phase for years for use in sunscreen (it absorbs ultraviolet wavelengths), some toothpaste (abrasive), and most significantly as paint (as a white pigment), but never with tight control of the size and size distribution. Because of it's widespread use and previous history, most chemical and optical data are available. The use of TiO_2 as a nanosize powder may be limited, but upon discovering methods of producing TiO_2 powders with controlled size and size distributions in the vapor phase, the same techniques can then be applied other ceramic powders.

The use of $TiCl_4$ did cause certain problems, however. One negative aspect of $TiCl_4$ was the recurring problem during these experiments of the reaction between $TiCl_4$ and water. The reaction rate with water is much faster than that with pure oxygen so whenever $TiCl_4$ came into contact with room air or any moisture, TiO_2 and HCl would be formed, creating serious corrosion and clotting problems throughout the system. Since control of the size distribution was strongly dependent on the temperature-controlled reaction rate, it was very important to maintain a dry reactor.

To prevent the reaction of $TiCl_4$ with water vapor and moisture, the reactant flows had to be passed through Drierite desiccant chambers before going into the reactor. These chambers were plastic tubes with connections at both ends and the chemical $CaSO_4$, commonly known as Drierite brand, in between. The $CaSO_4$ absorbed the moisture from the passing gases until it was saturated, but could be reactivated by being heated in an oven for several hours. In addition, the lines in the reactor were vacuum

pumped before startup to help remove any moisture. Any bead of water, if left during an experiment, would react quickly with passing $TiCl_4$ vapor and form a clot of TiO_2. Even with the care of evacuating the system and using the Drierite chambers, much of the reactor had to be cleaned or periodically replaced to remove contamination and areas damaged by acid. The effect of water contamination could be observed, using optical techniques discussed later in section 2.5, during an experiment as large "rocks" flowing through the reaction zone. These "rocks" were particles which formed before the reaction zone, often before entering the reactor, and then grew large before and during their journey through the reactor. When the reactor was free of contamination, the particles within the reaction zone appeared as a continuous sheet.

Caution also had to be exercised to prevent contamination of the reaction zone by water formed in the surrounding flame front since the reaction rate of $TiCl_4$ with water is much faster than that of $TiCl_4$ and oxygen. This concern is addressed again in the following section.

2.3 The Burner/Reactor

The centerpiece of the particle generation system was the wall free burner/reactor which consisted of a series of concentric tubes. The axisymmetric design was selected in hopes of creating a simple device which could be easily scaled up, as well as easily constructed from standard sizes of stainless steel tubing. This design allowed standard fittings to be used in joining the concentric tubes together, making the relative height of individual tubes adjustable.

As shown in Figure 3, the central stream carried the reactants, $TiCl_4$ and O_2, in dry argon. This stream passed through a 10 millicurie Po-210 alpha source within the burner designed to create a bipolar ion concentration. In the presence of an electric field, this

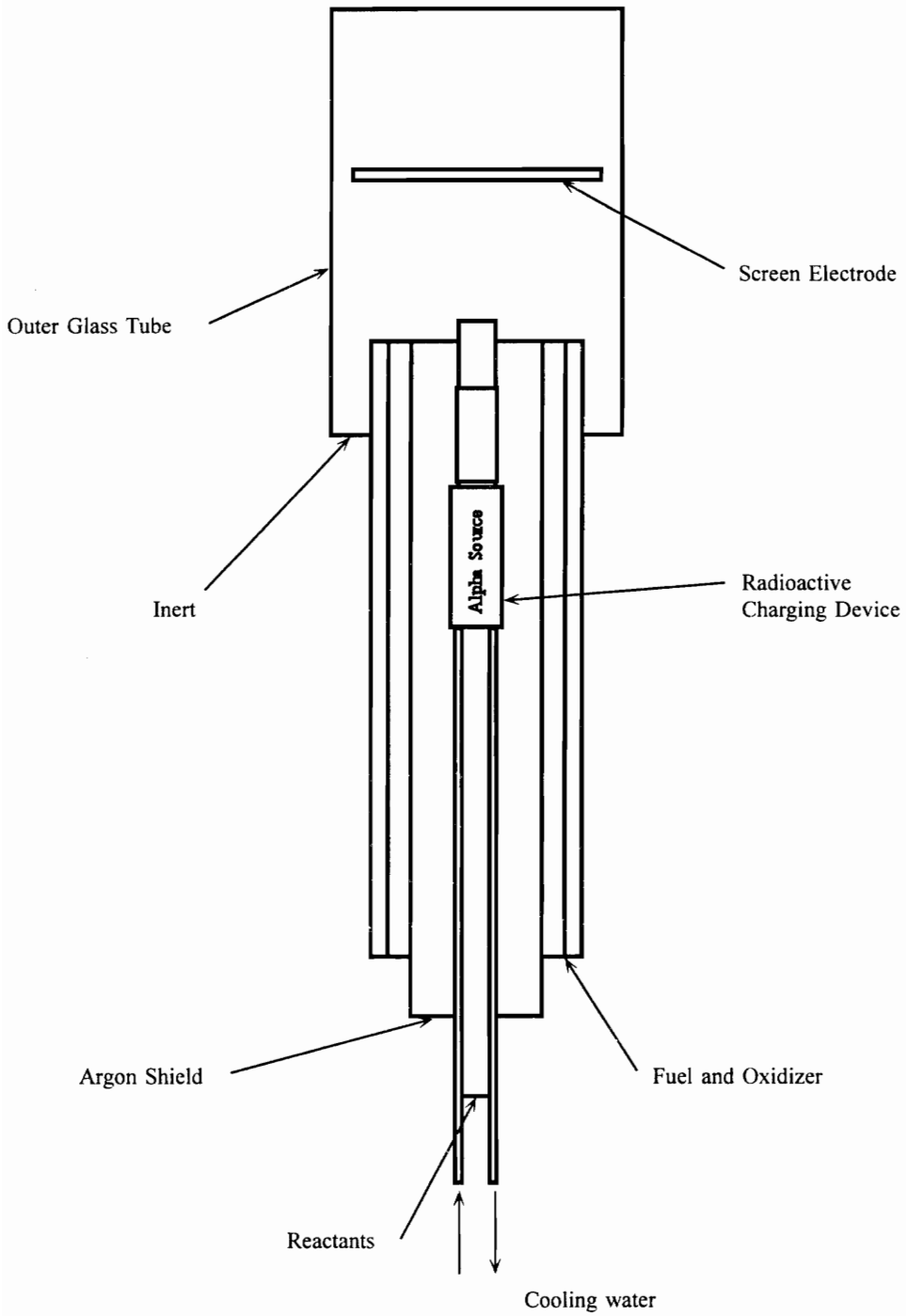

Figure 3. Burner/Reactor schematic.

ionization leads to either a unipolar-negative or unipolar-positive particle charging environment as discussed earlier in section 1.2.2.

The central tube was water cooled to prevent heat from conducting back down the reactor from the diffusion flame in the reaction area and starting the temperature dependent reaction early. Water ran in thin walled 1/8" diameter tubes inside of the central 1/2" diameter tube until the alpha source was reached, then ran around the outside of the alpha source and into a cooling jacket. The reactants remained cool until they left this cooling jacket and entered an 8 cm long stainless steel section, also 1/2" in diameter, leading into the reaction zone. Since heat could conduct back along this section, through trial and error the length of this section was adjusted so that particle inception occurred after the reactants left the central tube.

The $TiCl_4$ and O_2 were originally brought together at the base of the reactor to minimize the extent of reaction taking place before the reaction zone. Tests run to determine if the distance between where the reactants came together and the reaction zone was important showed no dependence on that distance. As a result, the two reactants were brought together several feet earlier in a small chamber to ensure complete mixing and then fed into the reactor.

The central stream was followed radially by a dry argon flow to shield the reactants from the flame products. This was necessary, as mentioned in section 2.1, to delay the introduction of the flame products such as water vapor into the reaction zone. This tube was 1.25" diameter stainless steel. The inner diameter, effectively, was 0.9" due to the presence of a ceramic liner. The white liner can be seen clearly in Figure 4. This liner prevented heat that conducted down the outer tubes due to the diffusion flame from radiating onto the central tube and heating the reactants prematurely.

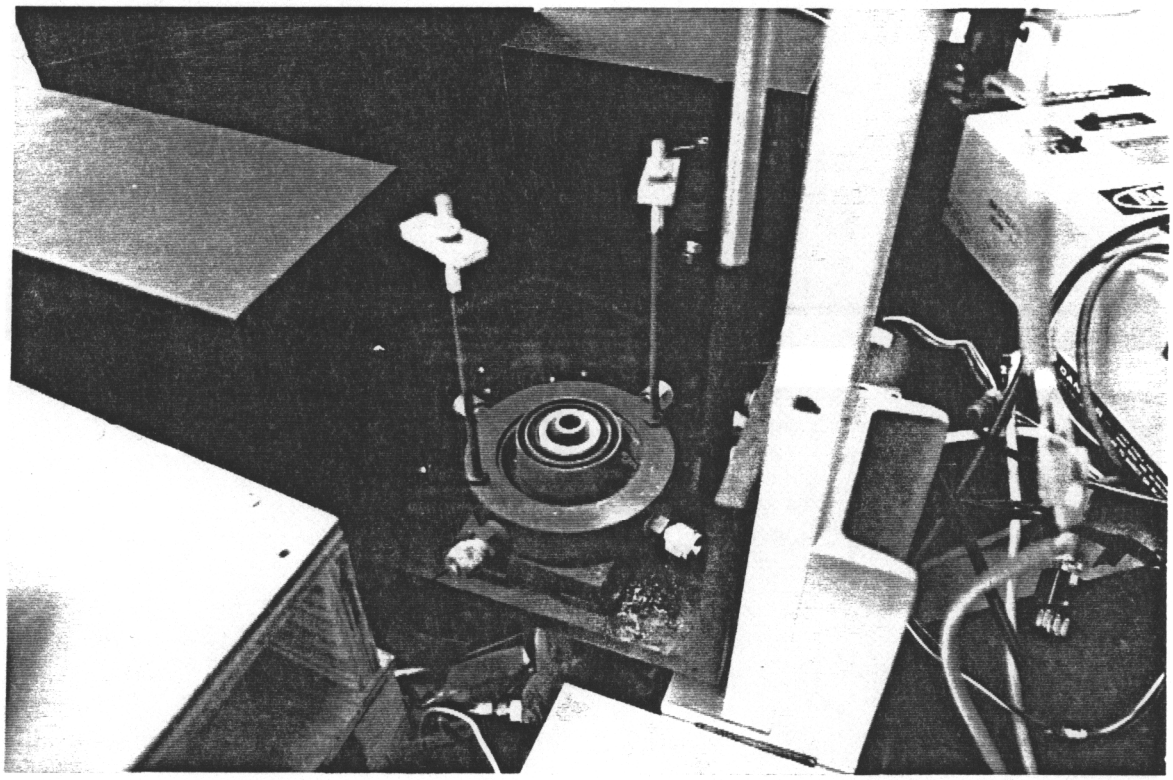

Figure 4. View of the co-annular burner/reactor from above.

Next, radially, were two streams containing the fuel and oxidizer for the H_2/O_2 diffusion flame. The inner tube had an outside diameter of 1.625" and the outer tube a diameter of 2.0". These two were the only that were not adjustable with respect to one another as gas-tight welds held both tubes at the bottom.

The last flow was a bypass around the outside of the diffusion flame. This flow of nitrogen helped to stabilize the flame and separate the flame from the Pyrex glass outer chimney wall.

Hydrogen was chosen as fuel for the diffusion flame to avoid the possibility of powder contamination by carbide formation. The burner was operated in two modes, one with H_2 in the inner fuel/oxidizer annulus and O_2 in the outer, and a second with O_2 in the inner annulus and H_2 in the outer. In both cases the flame was not allowed to close at the top. The flame attached itself to a doughnut shaped screen held 2.5" above the burner. This screen stabilized the flame and allowed access from the top for the insertion of thermocouples and sampling probes into the reaction zone. In the first configuration, with hydrogen nearest the center, the hydrogen from the diffusion flame mixed with oxygen from the reactant stream and started a second diffusion flame in the center of the reactor. Not only did this make temperature measurements difficult, but it directly introduced H_2O into the reaction zone. As a result, the second configuration with oxygen nearest the center was chosen for the final experimental runs. Thus, the concentration of oxygen available for the reaction was always in excess, and the limiting reactant was $TiCl_4$.

A ramped temperature field was used to make homogeneous nucleation take place at a slower and more controllable rate, forming a small concentration of new particles in the lower temperature zone and favoring surface growth onto existing particles over nucleation in the higher temperature area as demonstrated experimentally by Wu *et al*

(1987). The temperature field in the present work was measured using several BeO-Y_2O_3 coated [see Kent, 1970] Pt-Pt/Rh-13% thermocouples made from 0.003" wire. All these thermocouples were manufactured in the combustion lab by this researcher and had a bead size of approximately 0.009". Tests with uncoated thermocouples resulted in higher temperatures and often the destruction of the probe, justifying the coating of the bead. The measured field was found to be uniform radially within the reaction zone and ramped axially from 600 K to 1100 K, uncorrected for radiation. The leads of the thermocouple were kept parallel with the temperature isobars during measurement to minimize conduction errors. Typical temperature field and temperature fluctuation maps are shown in Figures 5 and 6 respectively.

The experiment was set up so that an electric field could be placed across the reaction zone from the burner/reactor to a downstream electrode. The doughnut shaped screen doubled as the downstream electrode. The burner was grounded and the electrode above the reaction zone was set to either high negative or positive voltage. This arrangement is similar to the charging experiments of Adachi *et al* (1992) where a bipolar region exists for several centimeters beyond the ionizing isotope followed by an environment which is unipolar, positive or negative depending on the field polarity.

2.4 Probe Sampling

Several techniques were evaluated for removing ceramic particles from the reaction zone as they formed. The techniques tried were sampling from the side with a cold finger probe, sampling from the top with a cold finger probe, and sampling from the top with a suction type probe. The cold finger sampling from above was determined to be the most reliable and least intrusive of these methods.

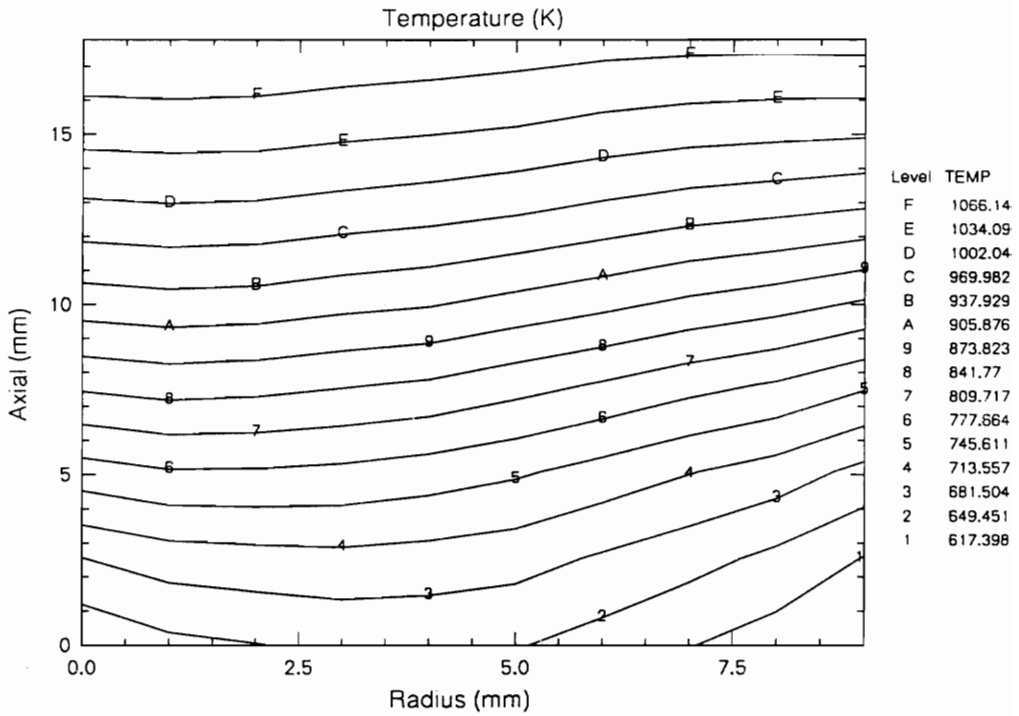

Figure 5. Temperature map of a typical laminar H_2/O_2 diffusion flame in the burner/reactor reaction zone.

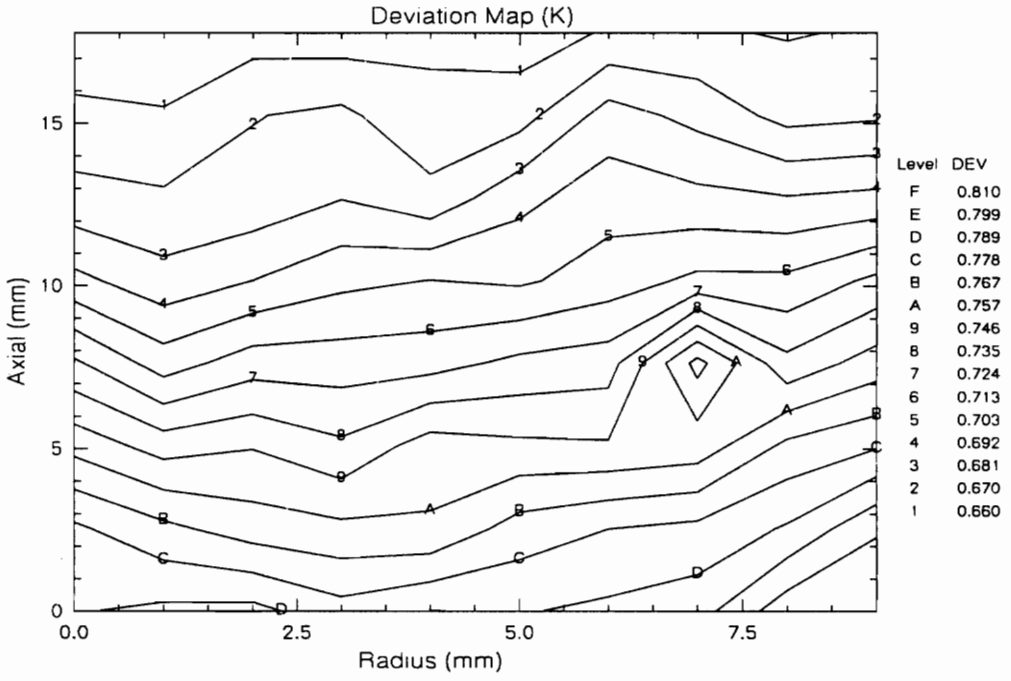

Figure 6. Standard deviations of the temperatures of the same typical H_2/O_2 diffusion flame demonstrating stability within the reaction zone.

2.4.1 Cold Finger Probe with Radial Insertion

A rapid insertion system that sampled particles from the side was tested in the reactor. A schematic is given as Figure 7. A translation stage held the probe at the desired height. This probe could be pushed into the reaction zone from the side through a short length of tubing. The tube prevented entrainment of air which would have made the reaction zone unstable while allowing the probe to start and finish away from the heat of the diffusion flame.

The probe was made of either a steel rod or a ceramic rod with a glass bead attached to the end. The probe material did not appear to have any effect on the collection of data in this configuration.

Particles were successfully collected using this insertion method and taken for analysis, as described later in section 2.4.4, under the Tunneling Electron Microscope (TEM). Particles collected under similar reactor conditions rarely appeared the same. It is believed that, because the probe had to travel through the flame as it entered and exited the reaction zone, the particle characteristics may have changed after they attached to the probe. The introduction of the probe into the reaction zone also caused a significant, non-symmetric, disturbance in the reactor.

2.4.2 Cold Finger Sampling from Above

A cold finger probe, shown schematically in Figure 8, was used to sample particles from the reaction zone by entering the reaction zone from above. The probe, either ceramic-glass or steel, was quickly lowered from the cooled sampling piece through a glass tube and into the reaction zone. The actual cooled sampling piece is shown in Figure 9a and the steel sampling probes are shown in Figure 9b. When the probe was dropped fully into the sampling piece, its end protruded beyond the glass rod a

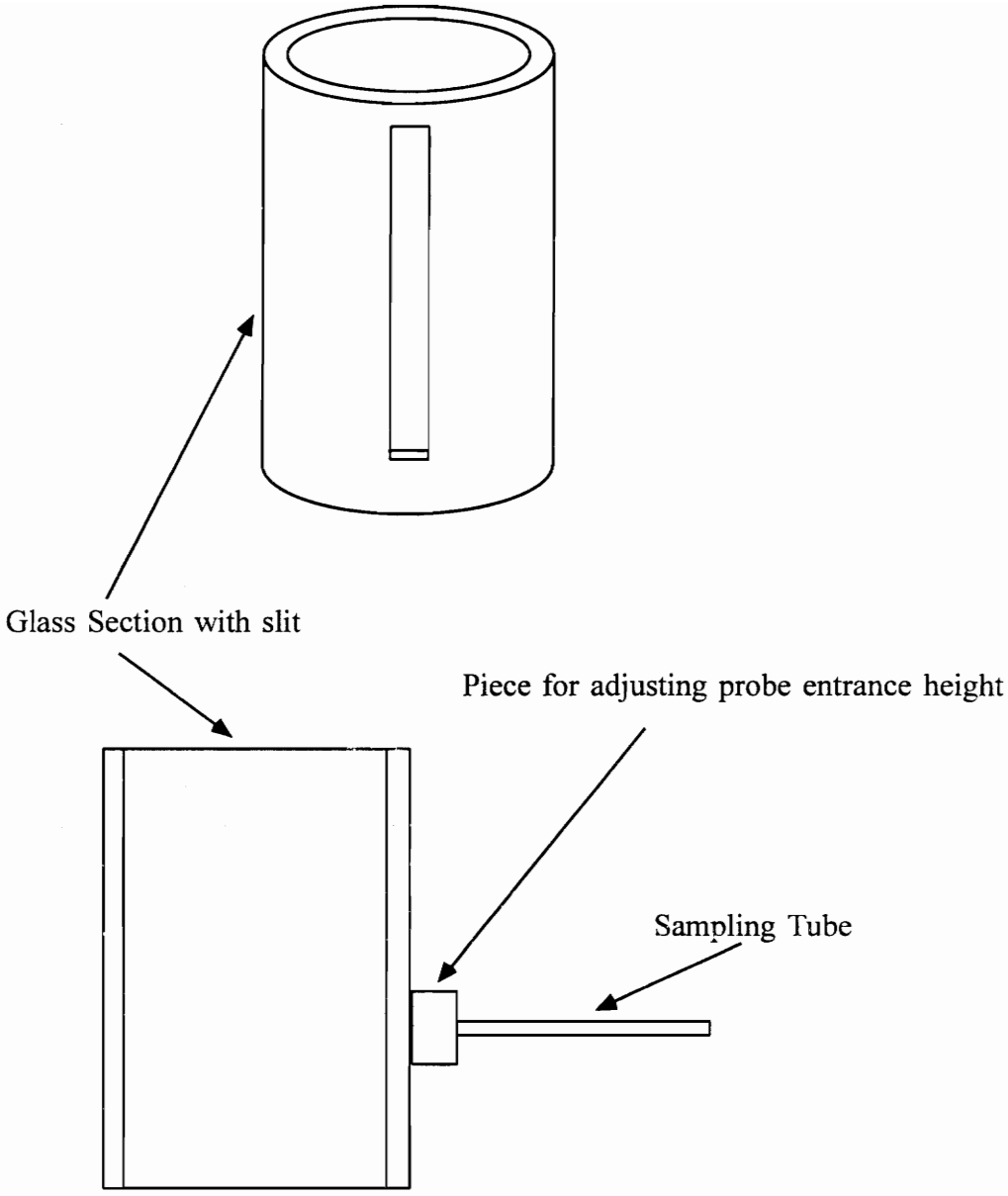

Figure 7. Particle sampling system where probe enters reaction zone from the side.

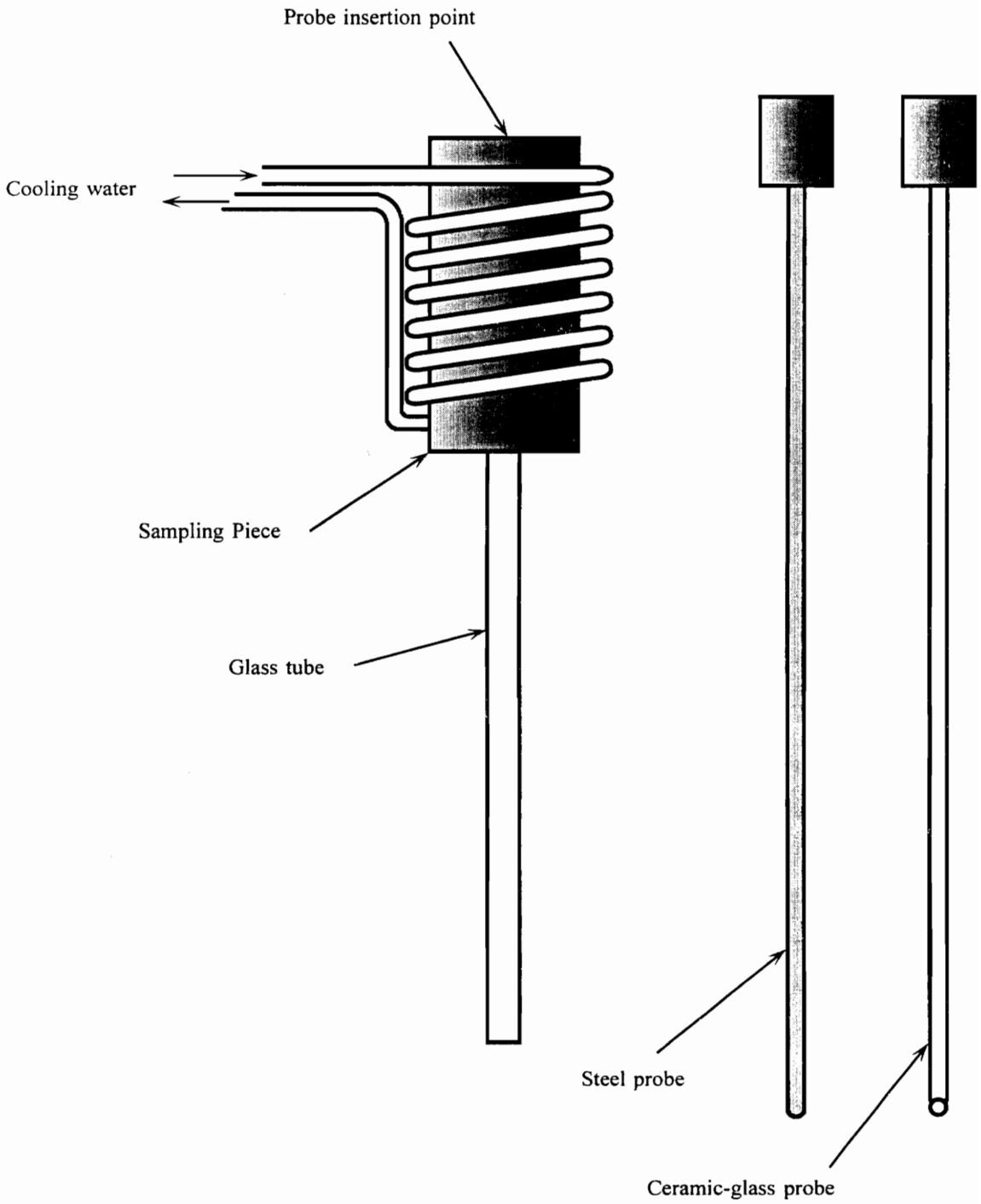

Figure 8. Cold Finger Probe.

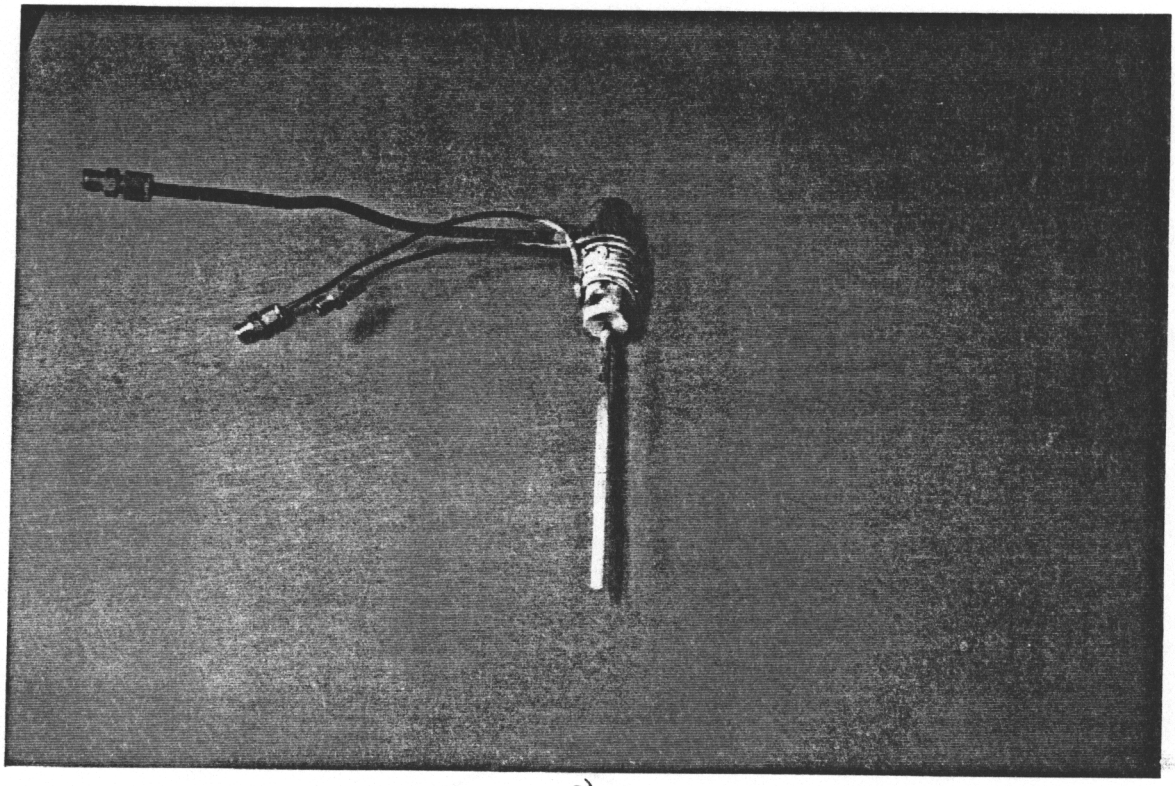

a)

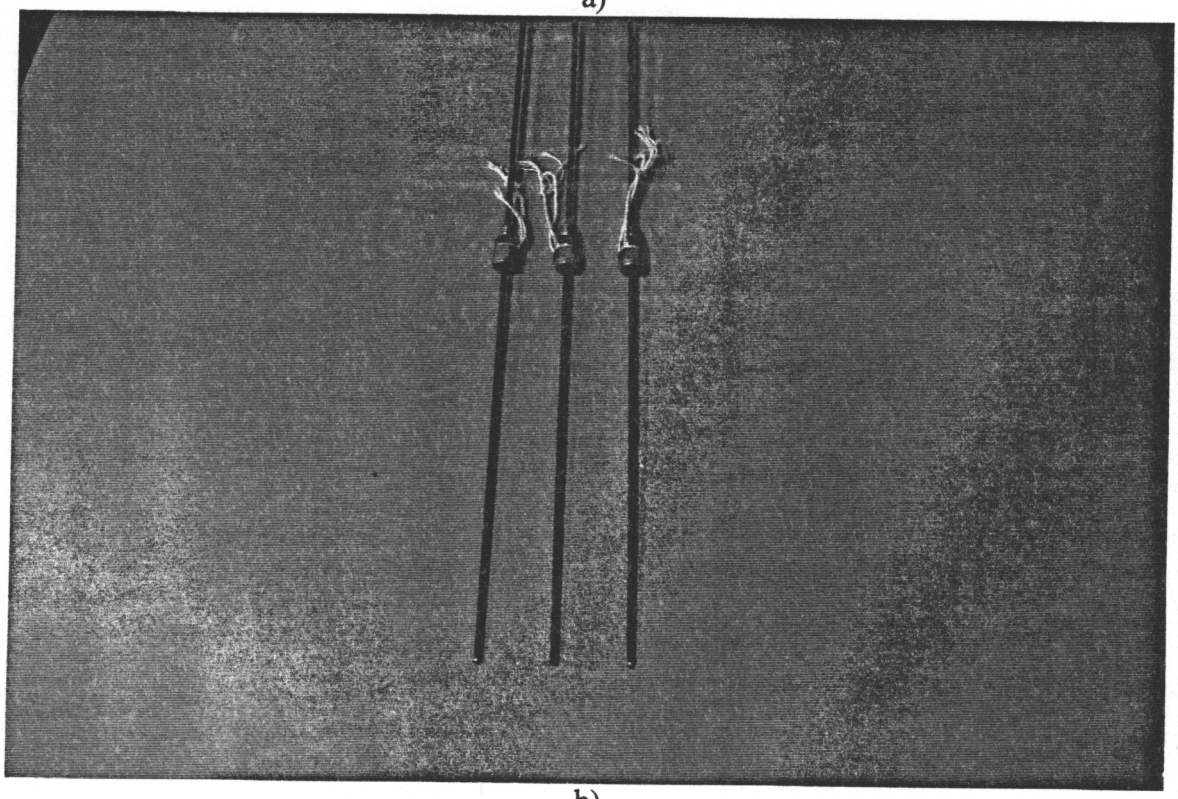

b)

Figure 9. a) Cooled sampling piece removed from experiment, b) Steel probes used for collection of particle samples.

few millimeters into the reaction area as seen in Figures 10a and 10b. When fully inserted the bottom of the probe was taken as the sampling height above the center tube of the reactor. The height of this apparatus was accurately determined by a computer-controlled linear stage. The probe apparatus is shown in position above the reactor in Figure 11.

Two probe materials were again tried in an effort to minimize the effect of the probe on the reaction and particle growth process. The ceramic glass probe was designed to have a minimal effect on the electric fields and the charged particles. However, no repeatable data could be collected with this probe when the electric field was on, so it was concluded that this probe may acquire a charge while in the reaction zone and either repel or attract particles resulting in erroneous particle samples. The steel probe was tested while grounded and while floating with no noticeable side effects on either the reaction zone or the collected data, so for simplicity all tests were run with the probe floating.

The disturbance caused by the introduction of the probe into the reaction zone in this configuration was less than in the "from the side" method, but was still seen to be significant, especially in cases when the electric field was on. The steel probe was able to produce repeatable results and was used to collect all the data. In comparable conditions, the particles appeared similar under the TEM.

2.4.3 Suction Sampling

With this method, a sample pump was used to draw part of the reactant/product stream out of the reaction zone and past a sample grid to collect the particles. The sample grid holder, shown in Figure 12, was to attract particles due to thermophoresis as the flow passed by. This is the method used successfully by Wu *et al* (1987). The probe evolved

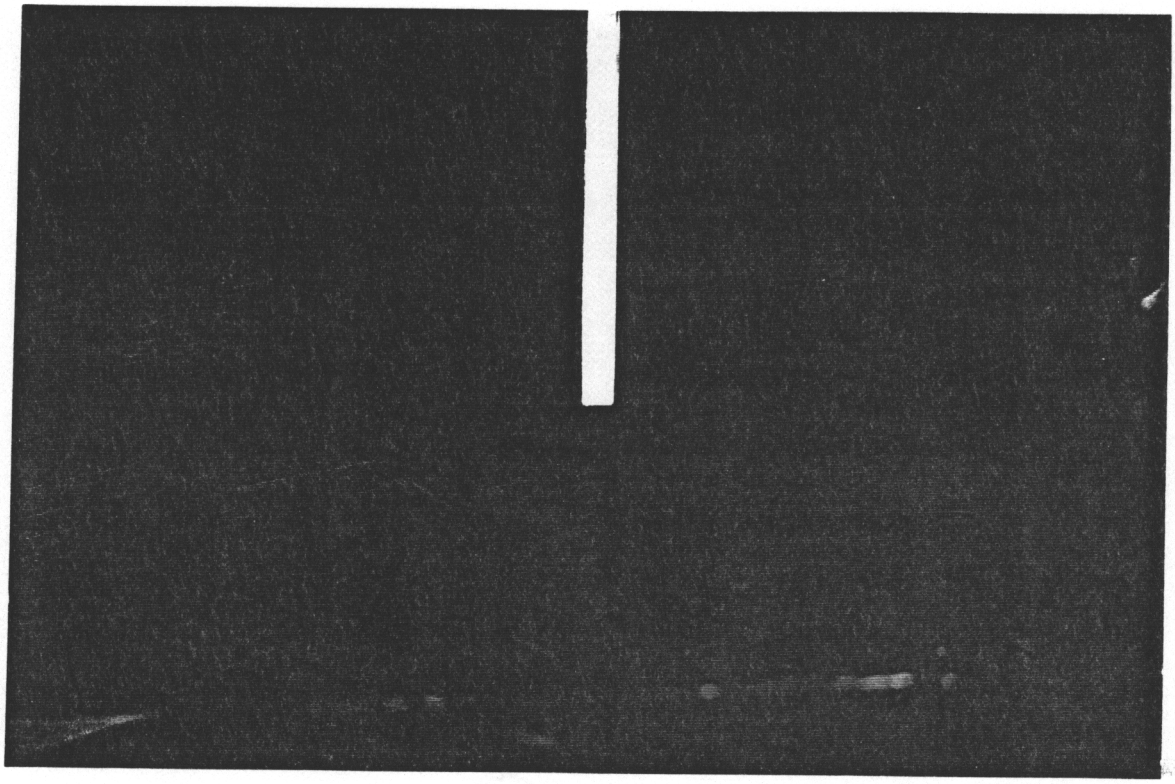

a)

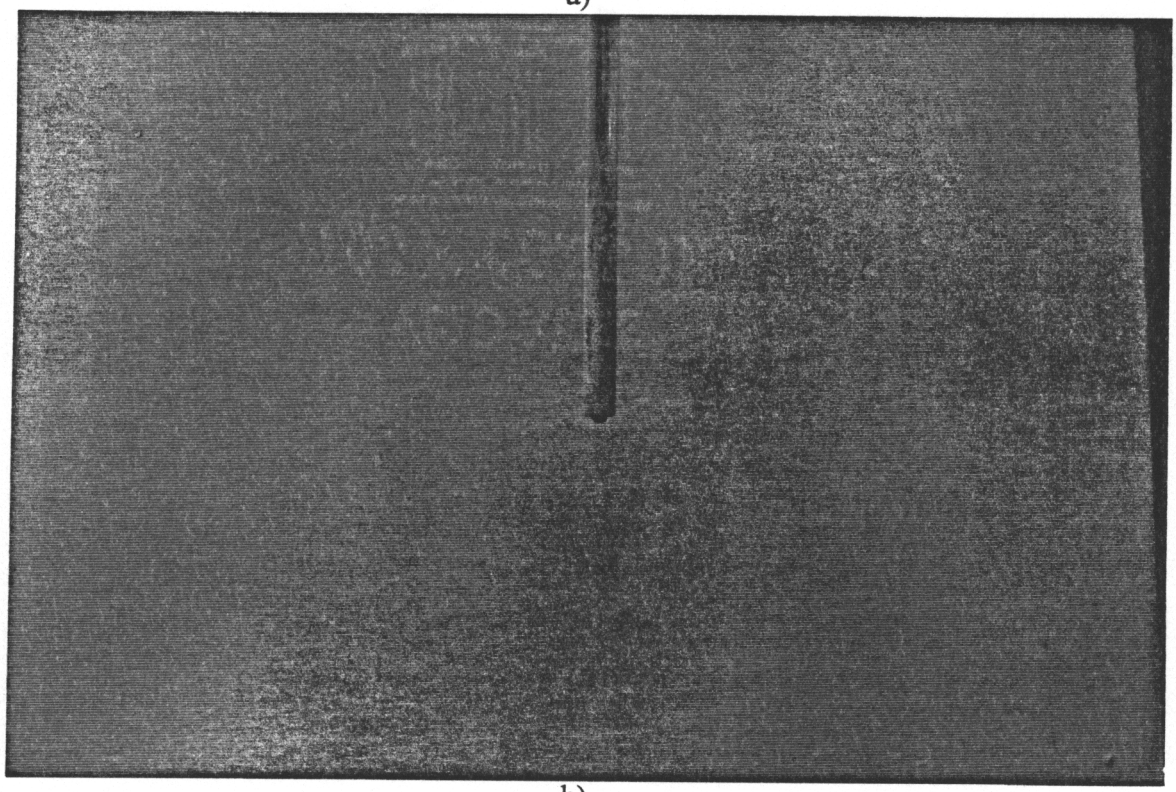

b)

Figure 10. a) Glass tube extending from the cooled sampling piece without probe inserted, b) Same view of glass tube with sampling probe in position.

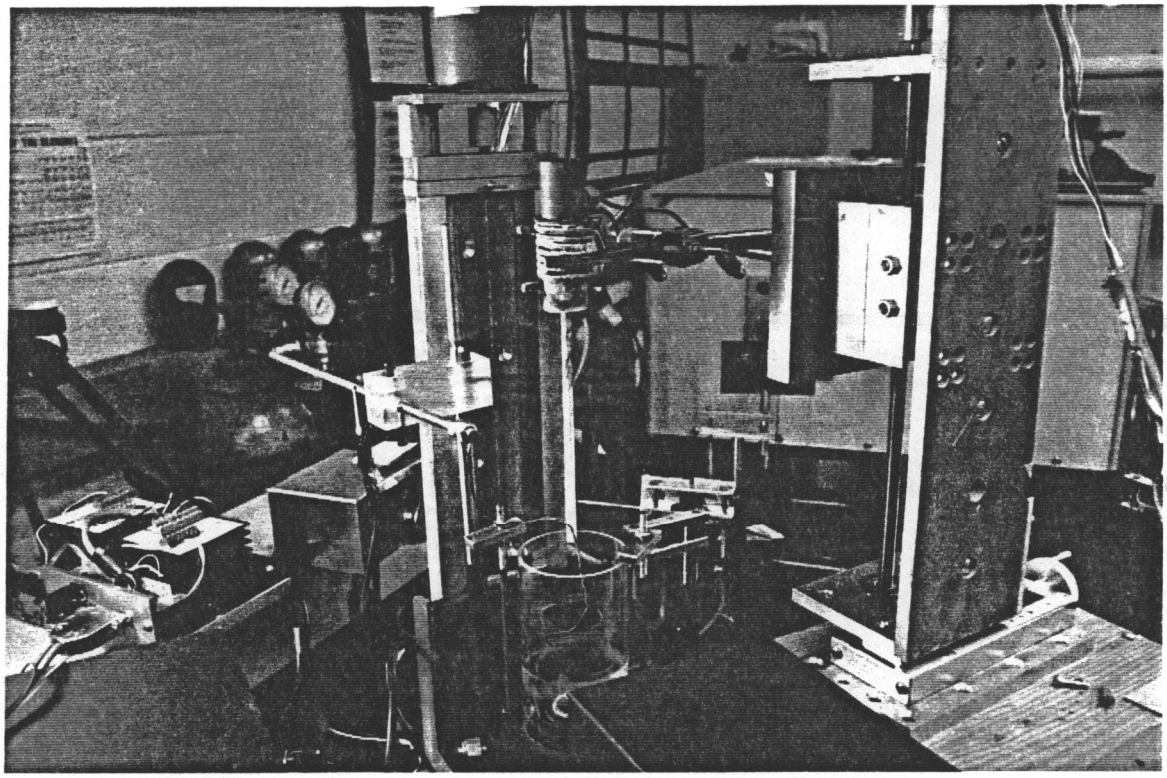

Figure 11. Particle sampling apparatus installed above the reaction zone.

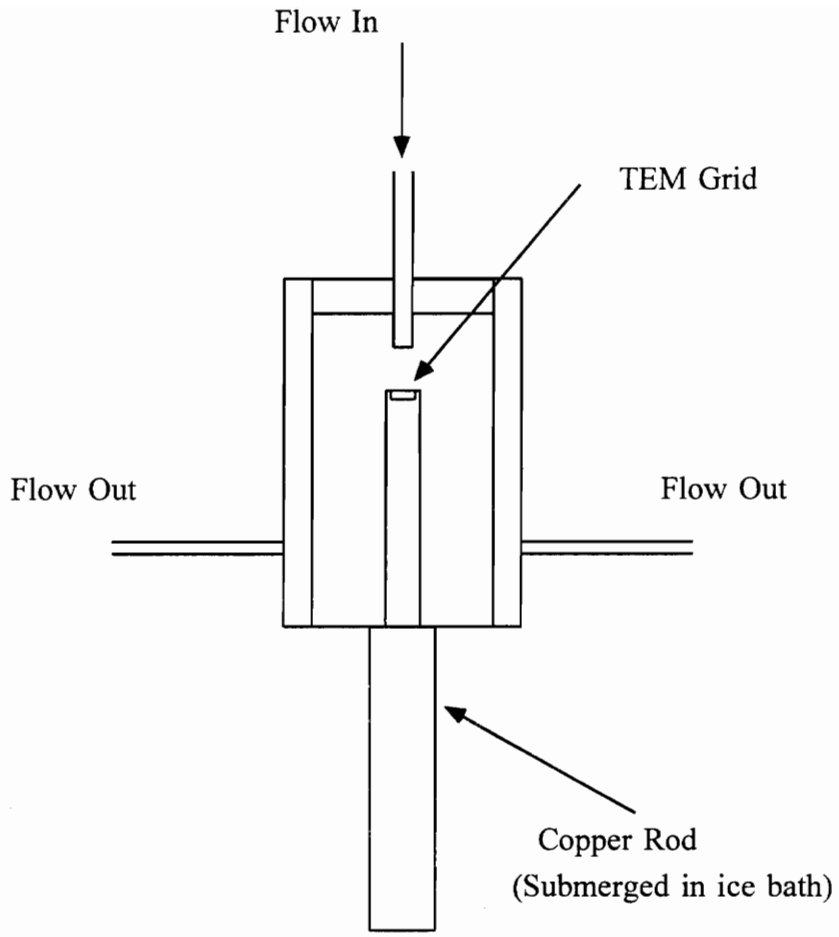

Figure 12. Grid holder for collecting particles from the passing flow using thermophoresis.

in three phases of complexity; first with a single tube, second with dilution air added, and last with a cooling jacket and dilution air.

The first probe, shown schematically in Figure 13a, consisted of a 1/8" stainless steel tube bent at 90° and placed in the reaction zone. A Thomas 2107 sample pump pulled the particles and reactants from the reaction zone. A bypass metering valve was placed just ahead of the pump to control the flow rate through the sampling probe. As the metering valve was opened, more flow came through the metering valve and less flow passed through the probe.

This configuration was unacceptable because the flow taken from the reaction zone was so hot that the TEM sample grids were being damaged. It was concluded that the temperature in the tubing between the reaction zone and the sample grid was high enough to allow significant growth of the forming particles. Also, the suction from the probe caused a distortion in the reaction zone.

A second probe was built, this time from glass, which would allow the addition of dilution gas at the sampling point. The flow rates of the dilution gas and suction in this probe, shown schematically in Figure 13b, could be adjusted so that no distortion was present at the sampling point. The dilution gas likewise cooled the sampled flow enough to prevent damage to the TEM sample grid. However, only a few large particles were collected on the grid. It was suggested that the flow may still be warm enough for the particles to continue growing between the reacting zone and the sample grid.

A third probe was built with a cooling jacket around the outside to keep the dilution gas from being heated as it entered the sampling area. Inside the cooling jacket the probe functioned the same as the previous version.

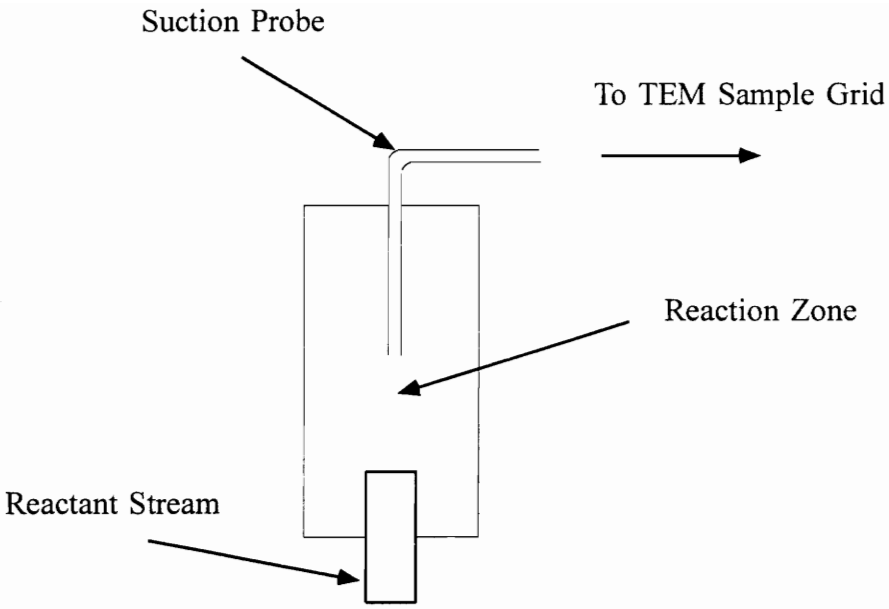

a)

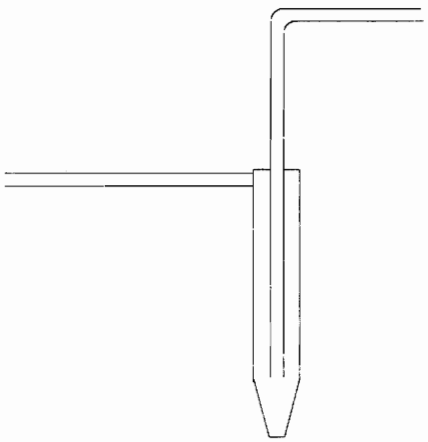

b)

Figure 13. a) Simple, single flow suction probe constructed from stainless steel tubing, b) Dilution flow suction probe constructed from glass.

Problems with condensation on the cooling jacket were solved by keeping the temperature of the water running through the probe high. This version of the probe, however, still only captured a few large particles.

The exact cause of this problem was not established but was suspected to be due to losses of smaller particles to the walls on the way to the sample grid or the smaller particles being carried past the sample grid while larger ones stuck.

2.4.4 Sample Grid Analysis

In the direct probe sampling of particles from the reaction zone, the probe was allowed to cool and then the particles were transferred onto a fine copper TEM grid with the aid of a special grid-holding device. The probe was lightly tapped against the grid holder, and the particles transferred from the probe to the grid. It could be seen under the microscope that the point on the grid where the probe actually hit was usually destroyed, but the particles were distributed successfully in the surrounding area.

The grids were made of thin copper which had hundreds of small square holes cut through it. One side of the copper grid was coated by a thin polymer film called FORMVAR. The particles deposit on this film, which is transparent to the electron beam, so they can be seen under the electron microscope suspended within the grid. If the film is destroyed, then the particles stick only to the copper grid and cannot be seen.

2.5 Optical Diagnostics

The first optical technique used was flow visualization using light scattering from ceramic particles within the reaction zone. A sheet of light, either from a He-Ne or Ar ion laser, was created by passing the laser beam through a cylindrical lens. This sheet extended from the exit of the central reactant tube to the wire stabilization screen-

electrode. Scattering from the particles was visible and allowed for easy qualitative observation of the macroscopic properties of the flow as well as acting as a diagnostic tool for centering the central reactant tube, adjusting the flow rates to maximize the reaction zone length, and positioning the sampling probe. Problems with water contamination and choking could usually be identified by watching for non-uniformities in the flow field before sampling particles.

In order to measure particle size non-intrusively, an optical diagnostic system was designed and installed. The system installed, shown schematically in Figure 14, is based on the Rayleigh theory of scattering and absorption by small particles, discussed in Appendix A. The present system uses two optical paths; one for extinction measurements and one for scattering. As the test section translates through the two beams, a full scan of the particle size characteristics within the reaction zone can be made. The windowed test section, shown in Figure 15, allowed light to pass through the test section along two separate paths, one 45° to the other.

The difficulty in measuring ceramic particles optically is that, in general, there is no light absorption in the visible spectrum. In the proposed setup, the extinction coefficient, K_{ext}, will be determined on one path using a UV source. Because scattering measurements are expected to be difficult to align in the UV, a second optical path using an Ar ion laser at 514.5 nm was set up to find the scattering coefficient Q_{vv}.

The UV source for the absorption path of the diagnostics, up to this point, has been a Lumonics excimer laser lasing at 337 nm. The laser cavity is filled with a mixture of N_2 and He. The laser produces a rectangular beam, about 2 cm x1 cm. The beam is initially trimmed by passing it through a mask with a 6 mm hole, then focused using a fused silica 497 mm focal length lens. A spatial filter, 1 mm in diameter, trimmed the

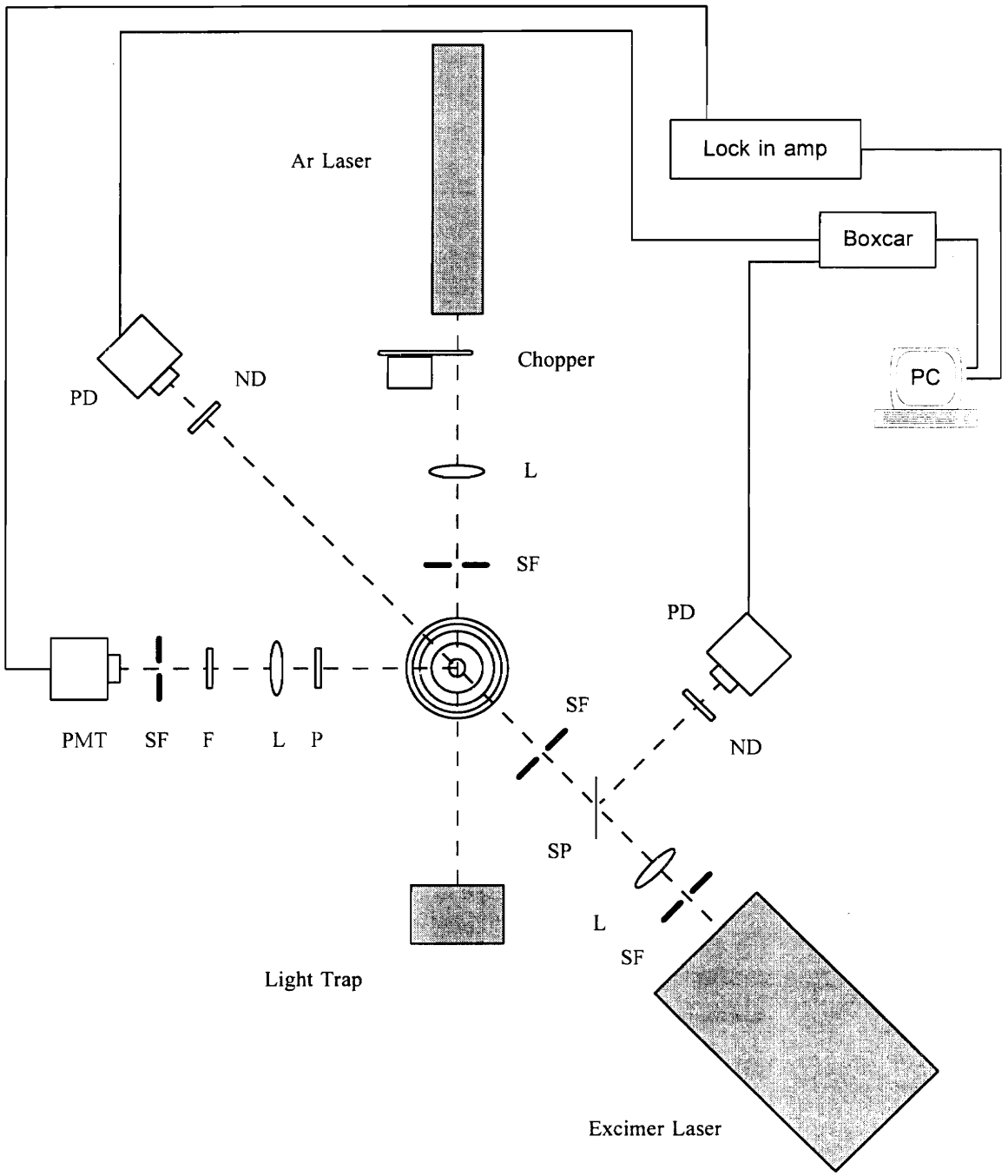

Figure 14. Optical diagnostic setup. Photomultiplier Tube (PMT), Photo Diode (PD), Spatial Filter (SF), Line Filter (F), Lens (L), Polarizer (P), Neutral Density Filter (ND), Splitter Plate (SP).

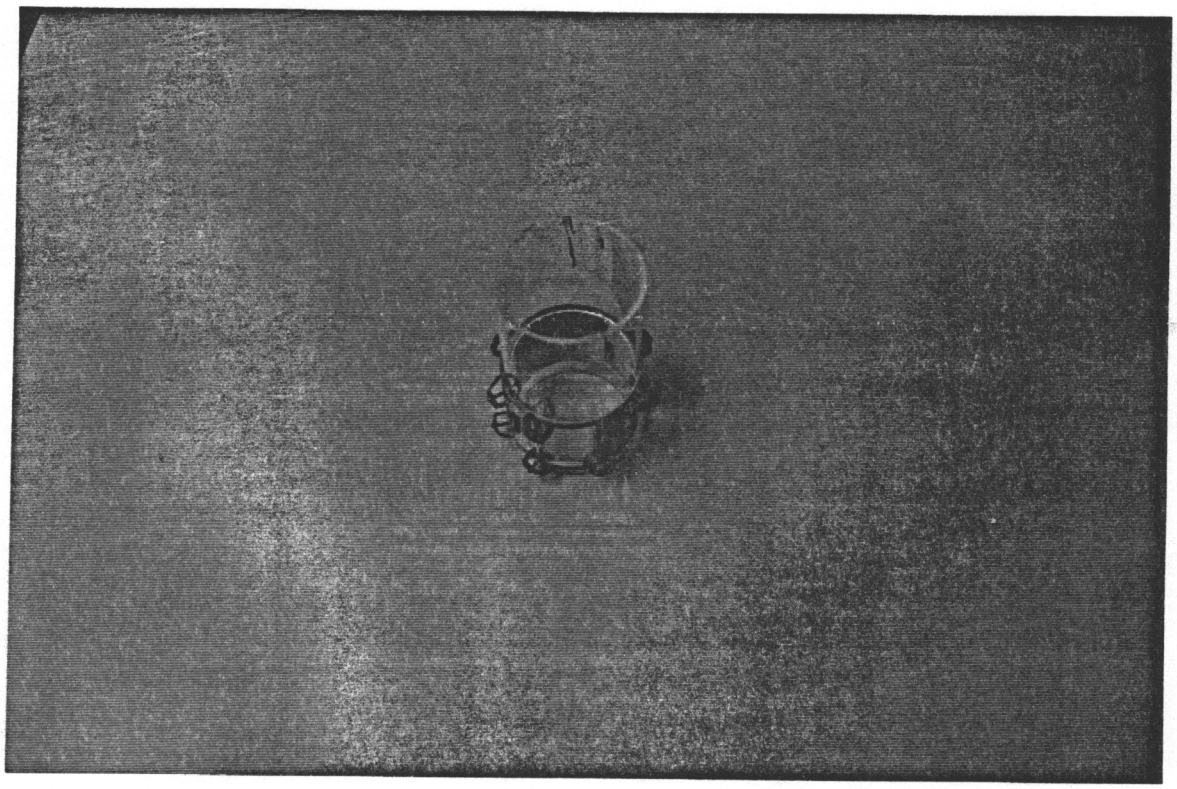

Figure 15. View above the assembled windowed test section. The visible beam would pass through from left to right with scattering optical components mounted in the lower middle of the picture. The UV beam would pass through from the upper right corner to the lower left corner, 45° to the visible beam.

beam again. The beam within the reaction zone appeared round and less than 1 mm in diameter when visualized with a fluorescing sheet placed in the beam path.

The UV beam was split just ahead of the final spatial filter by a flat glass plate. The reflected beam was directed into one photodiode, while the transmitted part of the beam proceeded through the reaction zone into a second photodiode, thus allowing measurement of I and I_0 for each pulse. This was necessary because the intensity of each pulse from the excimer laser is not exactly repeatable. Both photodiode circuits used the Hamamatsu type S1336-5BQ detector and were constructed according to the electrical diagram given in Figure 16. When the output was watched on an oscilloscope, both detectors responded to the laser signal, but the time responses were never exactly equal. The time response of the photodiode circuit is controlled mostly by the capacitance of C-1 (approximately 10 pF) and, even after some effort, the two detectors could not be completely matched. Both detectors had quartz neutral density filters in front of them to minimize interference from light sources and prevent saturation of the photodiodes by the laser pulse.

Due to the pulsed nature of the excimer laser, typical data acquisition such as an A/D board could not be directly employed. The data acquisition rate of the available A/D boards was not fast enough to capture the 10 nanosecond laser pulse, so a boxcar averager was installed to measure the outputs from the photodiodes. The use of the boxcar averager and the excimer laser will be discussed further in the results section 3.5.

The second optical path, used to measure scattering from the particles, employed an Ar ion laser operating on the 514.5 nm line. The beam was passed through a polarization rotator to ensure vertical polarization of the incident light. This was followed by a Stanford Research mechanical chopper wheel operating at 150 Hz to

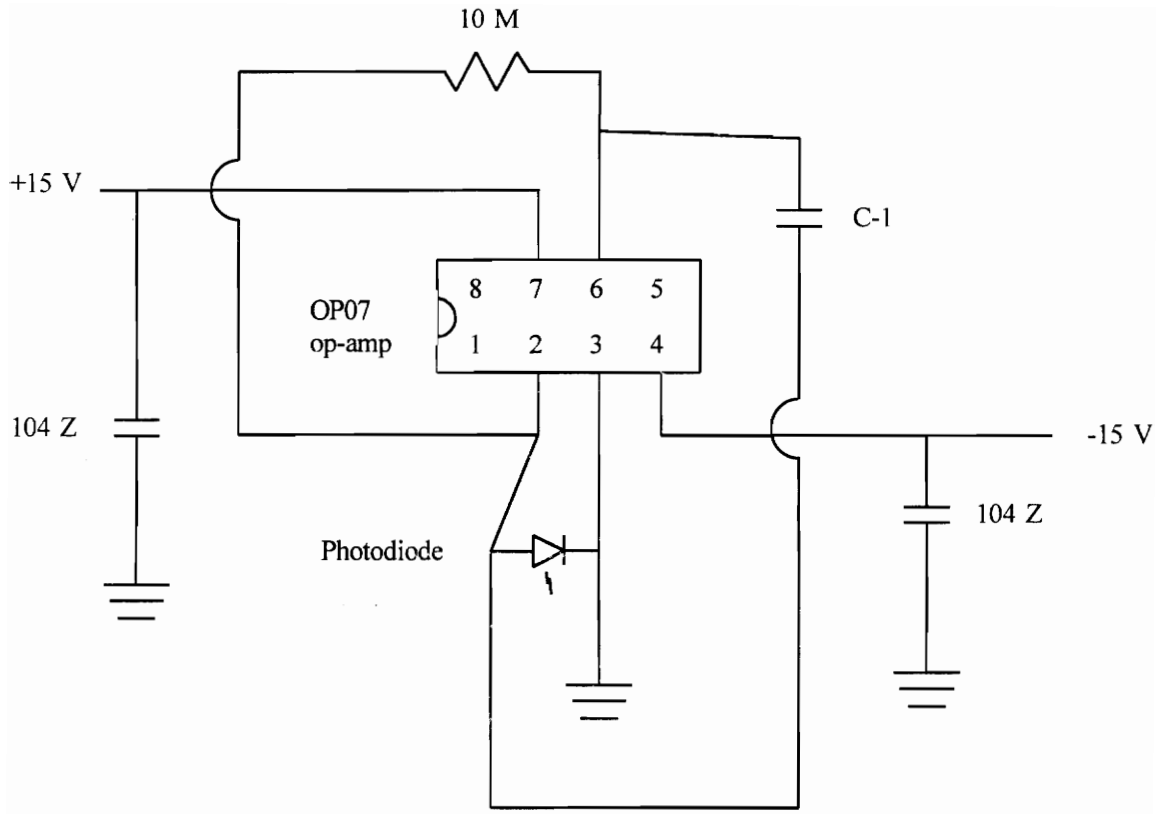

Figure 16. Photodiode amplification circuit.

eliminate noise from the flame, a 500 mm focal length lens, and a 1 mm spatial filter before entering the reaction zone.

The light scattered by the particles was measured with a Hamamatsu 1P28a photomultiplier tube (PMT) powered by a Pacific Instruments power supply. The PMT was typically operated between -800V and -1000V. The optics ahead of the PMT included, in order from the test section to the PMT, a polarizer on a rotating mount, a light tight tube housing a 147 mm focal length lens, a 514.5 nm line filter, and a 0.8 mm spatial filter. The test section was approximately 300 mm from the lens. Care was taken to focus the test volume onto the spatial filter using 1:1 imaging.

The scattering optics were tested using gases of known properties, in this case N_2, CH_4, and C_3H_8 gases. The ratio of the differential scattering cross sections of these gases can be calculated if the incident wavelength, index of refraction, and depolarization ratio are known. The accuracy of the optics can be verified by measuring these ratios experimentally and comparing them to the calculated ratios. Measurement of the gases cross sections also serves to calibrate measurements taken during an experiment.

Figure 17 shows the various optical components as installed around the experiment.

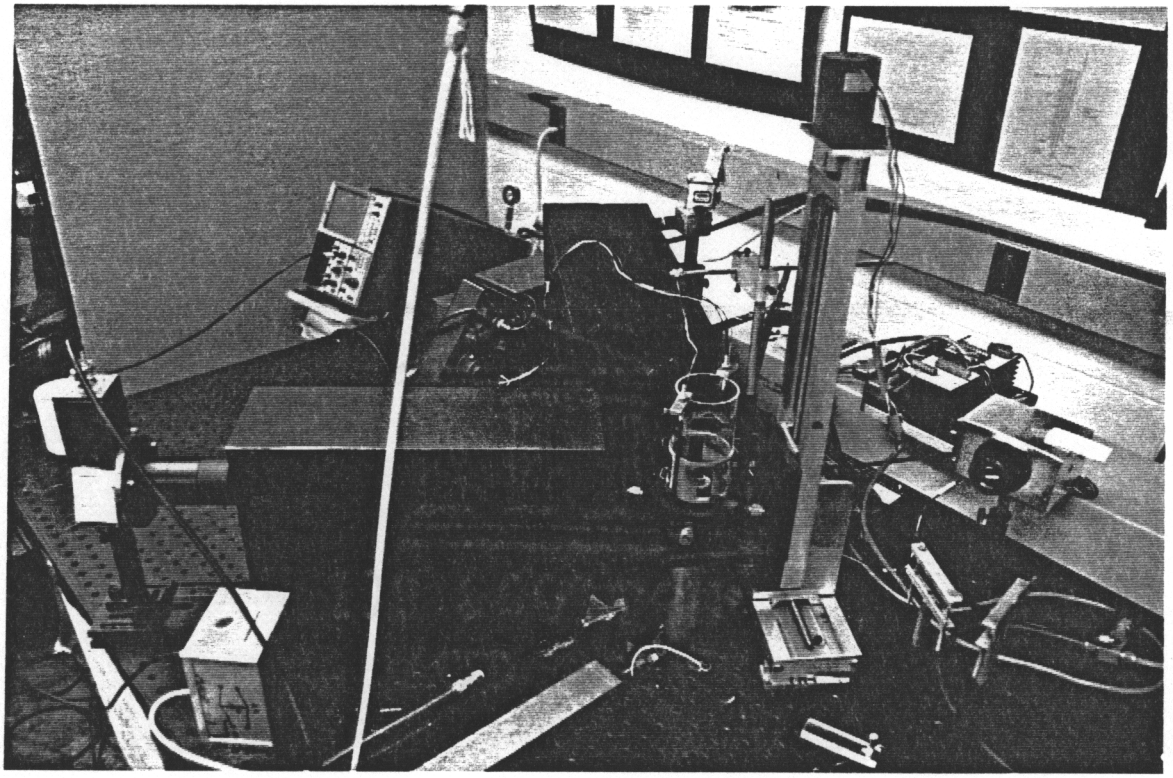

Figure 17. View of the experiment from above showing the location and setup of various optical components as well as the windowed test section. The excimer laser beam enters from the lower right-hand corner while the Ar ion beam enters out from beneath the hood in the top-middle of the picture.

3 Results and Discussion

3.1 Introduction

In this section the results of the experimental work will be presented and discussed. The experimental data collected, in addition to experimental conditions such as flow rates and temperatures, consists of TEM negatives and observed behavior of the flow within the reaction zone. The parameters varied during these experiments were the reactant concentrations and the electric field configuration.

3.2 Temperature Field

In order to maintain a constant temperature field throughout all the experiments, the flow rates governing the diffusion flame and shield flows were always the same, and the overall flow rate in the central tube of the reactor was kept constant for all conditions. When reactant concentrations were changed, argon was used to balance the flow rate. The addition or subtraction of this argon balance has no noticeable effect on the temperature profiles because the flow was nearly 100% argon. The measured field, as described in detail in section 2.3, was found to be uniform radially within the reaction zone and ramped axially from 600 K to 1100 K. A typical temperature field and temperature fluctuation map was shown in Figures 5 and 6 respectively.

3.3 The Electric Field and Particle Charging

The electric field placed across the reaction zone during the reported experiments was either -480 V, -900 V, or +1040 V. These three settings represent the highest negative voltage that could be applied across the reaction zone, a smaller voltage to demonstrate the effect of varying voltages on particle growth, and the maximum positive

voltage that could be applied across the reaction zone. The magnitudes of the voltages used were determined by the point where, as the voltage was increased, instabilities formed on one side or the other of the reaction zone and started an oscillation in the flow. This instability was believed to be caused by charged particles attempting to follow electric field lines which cross the streamlines in the flow itself.

Since the downstream electrode was kept 6.35 cm above the burner, the electric field strength was between 75 V/cm and 164 V/cm. Hardesty & Weinberg (1972) used a much stronger field in their work. However, in the present experiment no attempt was made to measure the ion number density, so a direct comparison between the work of Hardesty & Weinberg (1972) and this work is irrelevant.

The reaction zone was visualized (as explained earlier in section 2.4) with a sheet of laser light. Figure 18 shows two photos of the reaction zone with the particles illuminated by the argon ion laser, one with no electric field applied and the other with a high positive voltage applied to the downstream electrode. When no electric field was present (Figure 18a), scattering from forming particles was present beginning about 10 mm above the center reactant tube. The scattering zone extended about 6-7 mm until it reached the recirculation zone.

When no particles were present, no effect was observed on the flame or the flow field when the electric field was applied. With the particles present, significant differences could be seen between the positive and the negative case. Because of the clear reaction of the particle laden flow to the applied electric field, it was concluded, at the time, that a significant portion of the particles were acquiring charges.

When a positive voltage was applied to the downstream electrode, the point of particle inception pulled farther downstream; the zone where scattering was observed was higher above the central tube and shorter and less intense (Figure 18b). When a negative

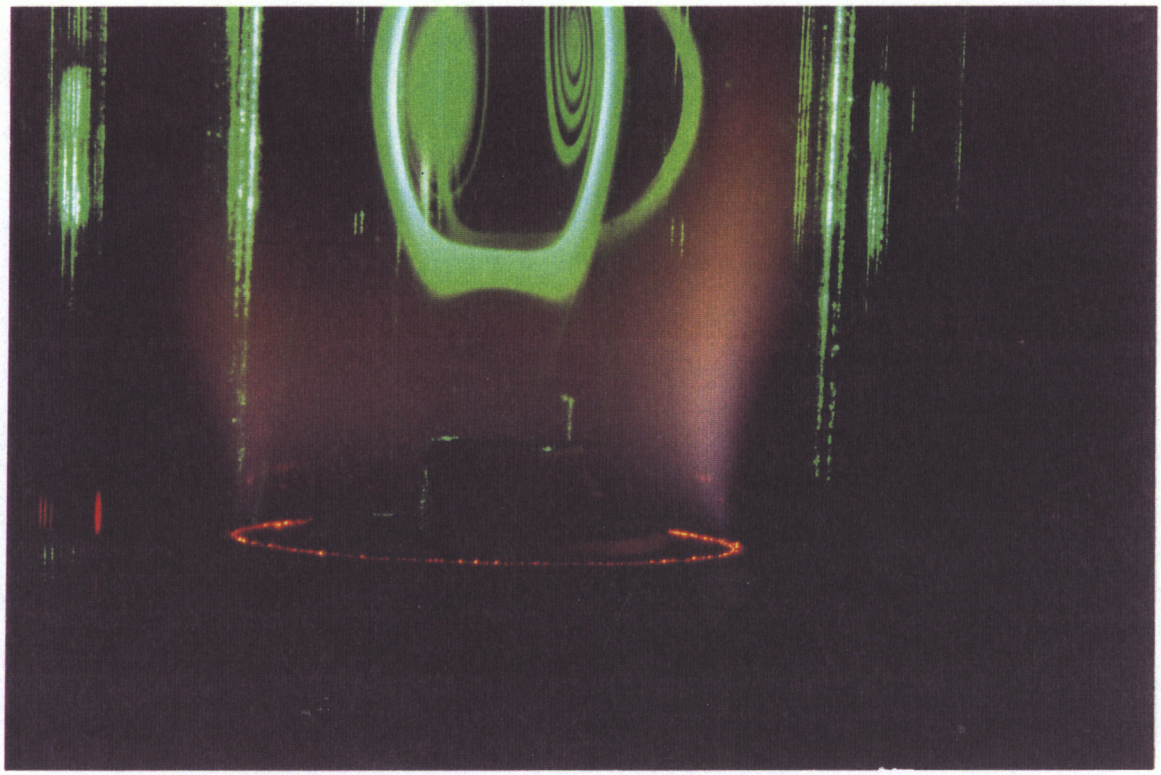

a)

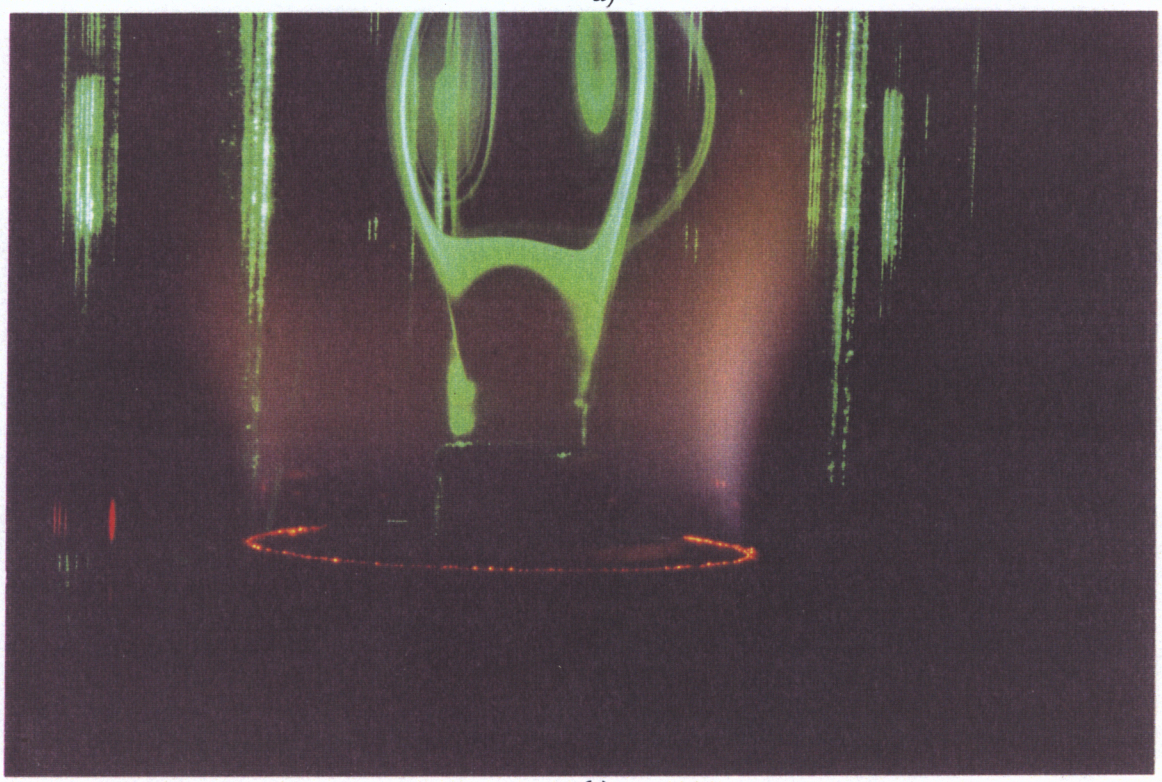

b)

Figure 18. Reaction zone illuminated by Ar laser sheet. a) No electric field is present. b) Positive electric field applied across reaction zone.

voltage was applied, the scattering zone moved upstream and spread out, becoming longer and brighter. The flow was always able to withstand higher voltages in the positive case. The maximum voltage attainable was also dependent on the position of the sampling probe within the reaction zone. The flow was able to withstand higher negative voltages when the probe was higher above the burner.

It was the intention when designing this reactor that, when the burner/reactor was grounded and the electrode was at a positive voltage, negative ions formed by the radioactive ionizing source would be pulled downstream by the positive electrode while positive ions would lose their charge to the grounded walls of the burner. In that case charged particles themselves would be expected to be accelerated along electric field lines towards the electrode. The greater the electric field, the faster the charging and particle acceleration downstream. If the downstream electrode was negative, negative ions would lose their charge to the walls while positive ions would be drawn downstream to transfer their charges to forming particles. The particles would again be accelerated towards the electrode. However, in both cases the particles reacted to the applied electric field as if they were negatively charged.

After all the experiments had been completed, the actual effect of the Po-210 alpha source on the system was called into question by these observations so additional tests were run with and without the device in place. The tests were run at identical conditions except for the presence of the alpha source. In both cases the particles reacted as negatively charged.

The possible explanation for these results involves the physics of the ionization process and the chemical kinetics of the forming TiO_2 particles. The gas in which the reactants were traveling in this experiment was mostly argon. When argon atoms are ionized, they lose an electron leaving an Ar+ ion and a "free electron". A gas such as

oxygen will form a pair of ions, one positive due to the loss of an electron and one negative due to the acquisition of the free electron. In the experiments of Adachi *et al* (1992) these ion pairs were present since his particles traveled in air. In the present experiment very few ion pairs would have existed. The large difference in mobility between the electron and the Ar+ ion may result in slower positive charging or more rapid ion recombination than in the case of the ion pairs where the mobility of the positive and negative ion are very similar. The net result was severely diminished effectiveness at transferring a charge to any atoms or molecules in the stream.

The fact that the particles within the reaction zone react to the applied electric field without the radioactive ionizer in place may be explained in several possible ways:

1. Charges originating in the washing bottle where $TiCl_4$ vapor is added to the reactant stream carry through the experiment and into the reaction zone. This situation might occur, for instance, if there were a grounded metal atomizing nozzle present. Since the reactant in the present study is in the vapor phase and enters the reactant stream from a glass flask, this seems an unlikely explanation.
2. Frictional charging due to flow through the experimental apparatus. This option was not thought to be likely due to the lack of particles prior to entering the reaction zone. However, Sanzone (1994) suggested that it was still possible for electrons from the metal tubing to be acquired by a passing gas stream since the reactor was grounded. This ground could provide a steady source of electrons. But, because the reactant stream is mostly argon, the likelihood of significant electron acquisition seems low. The only way to truly know is to measure the ion concentration of the reactants before they enter the charger and reaction zone.
3. Charges on the particles may be attributed to the reaction between $TiCl_4$ and O_2. The chemical kinetics of the oxidation of $TiCl_4$ to TiO_2 as presented by Pratsinis *et al*

(1990a) did not include any charges left on particles after the reaction was completed. However, electro-negative intermediate radicals which are known to adsorb on the surface of the solid phase TiO_2 particles, like OCl, may temporarily cause the particles to react to the applied electric field as if negatively charged. Sanzone (1994) and Davis (1994) both agree that this is a possible explanation for the observed behavior. Both stressed that knowledge about the ion concentration of the reactant stream before it enters the reactor and charger would be required to establish any explanation with confidence.

3.4 Probe Particle Sampling

The quantitative results from these experiments were measured by taking particles from the reaction zone, examining them beneath the TEM, and measuring the average diameter and standard deviation in each case. Many samples were taken from the reaction zone at several heights above the reactor, both with and without the high voltage, and at different reactant concentrations. Table 3 is a summary of the conditions for which samples were acquired. Conditions with a * indicate that the condition was run with and without the alpha source. The volumetric flow rate in the center tube was kept constant for all the experiments, so the velocity and temperature profile was assumed to be equal in all cases. The flow rate for gases in the diffusion flame was 110 ml/s for H_2 and 90 ml/s for O_2.

Table 3. Experimental Conditions

Condition	Height (mm)	Voltage (V)	Flow Rates (ml/s)		
			$TiCl_4$	O_2	Ar
1	10.2	No	3.2	2.7	1.6
2*	10.2	No	1.6	2.7	3.2
3	10.2	HV-480	1.6	2.7	3.2
4	10.2	HV+1040	1.6	2.7	3.2
5*	12.7	No	3.2	2.7	1.6
6*	12.7	No	1.6	2.7	3.2
7	12.7	HV-900	1.6	2.7	3.2
8*	12.7	HV+1040	1.6	2.7	3.2
9	15.2	No	3.2	2.7	1.6
10	15.2	No	1.6	2.7	3.2

Table 4. Average Diameters at Experimental Conditions

Condition	Average Diameter (nm)	Standard Deviation (nm)
1	18	7
2	20	4
3	20	4
4	23	4
5	39	5
6	22	5
7	17	6
8	19	7
9	47	7
10	20	5

In Figure 19 conditions 1 and 5 are compared to demonstrate the effect of height above the burner on the size of sampled particles. The particles in condition 5 are clearly larger than in condition 1 with the only experimental variable changed being the height above the reactor central tube. The average diameter of the particles in each condition is given in Table 4. Additional information on the size data is given in Appendix B.

A comparison between conditions 1, 5, and 9 shows a clear trend of increasing diameter with height above the central tube. Comparison of 2, 6, and 10 does not show such an increase. The diameter, as demonstrated by Figure 20, stays approximately the same at each height, implying that the growth takes place quickly and that no significant change in the size takes place after that initial growth in the low $TiCl_4$ concentration cases.

In Figure 21, conditions 5 and 6 illustrate the effect of $TiCl_4$ concentration on the size of the sampled particles. Figure 22 shows another comparison between condition 5 and 6, this time at higher magnification. The increase in diameter is significant and consistent, as shown in Figure 23 by a comparison between conditions 9 and 10 where again the only variable changing is the concentration of $TiCl_4$.

An electric field was present in conditions 3,4,7, and 8. In Figures 24, 25, and 26, two separate samples from condition 3 are compared against condition 2, where there was no electric field but all other conditions were the same. The size and shape of the particles are, by observation, the same in both cases. In Figure 27, condition 4 is compared against condition 2, where again there is no significant difference between the case of the electric field and the case without the electric field. Figures 28 and 29 show the comparison between condition 7, with a negative electric field, and no field condition 6 and the comparison between condition 8, with a positive electric field, and 6 respectively.

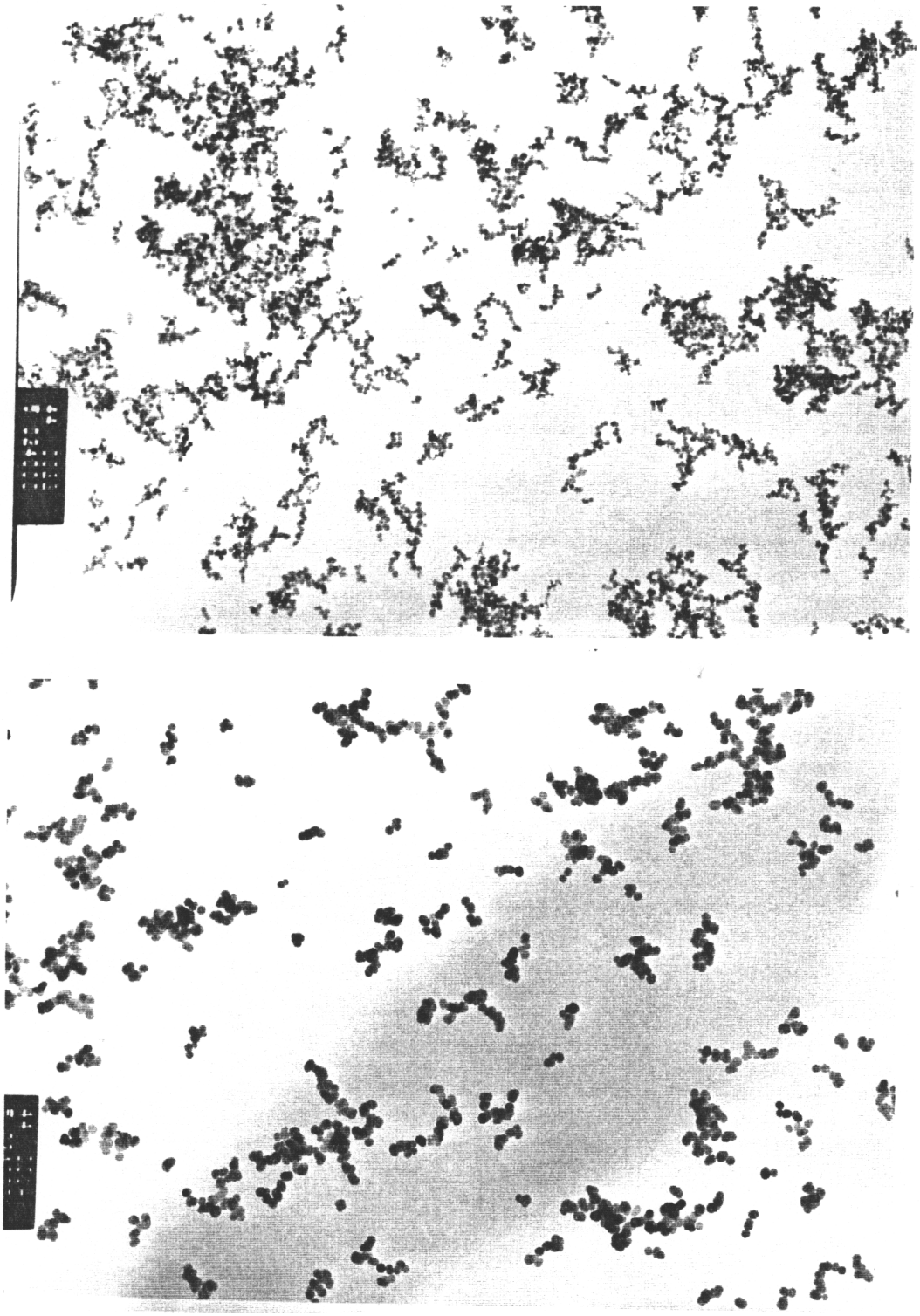

Figure 19. (top) Condition 1, Height = 10.2 mm, No Voltage, $TiCl_4$ 3.2 ml/s, 24K
(bottom) Condition 5, Height = 12.7 mm, No Voltage, $TiCl_4$ 3.2 ml/s, 24K
Scale Bar = 560 nm

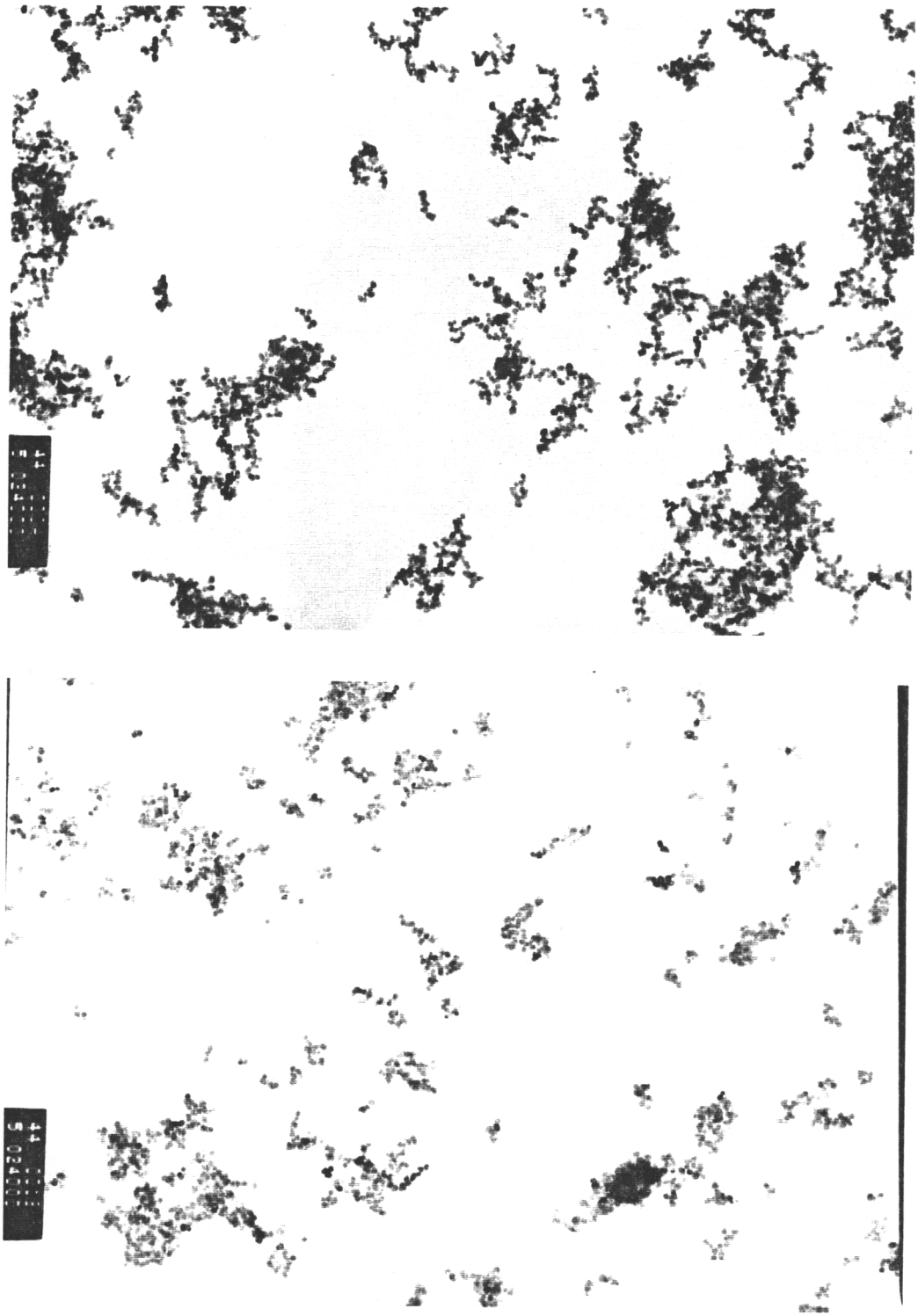

Figure 20. (top) Condition 6, Height = 12.7 mm, No Voltage, $TiCl_4$ 1.6 ml/s, 24K
(bottom) Condition 10, Height = 15.2 mm, No Voltage, $TiCl_4$ 3.2 1.6 ml/s, 24 K
Scale Bar = 560 nm

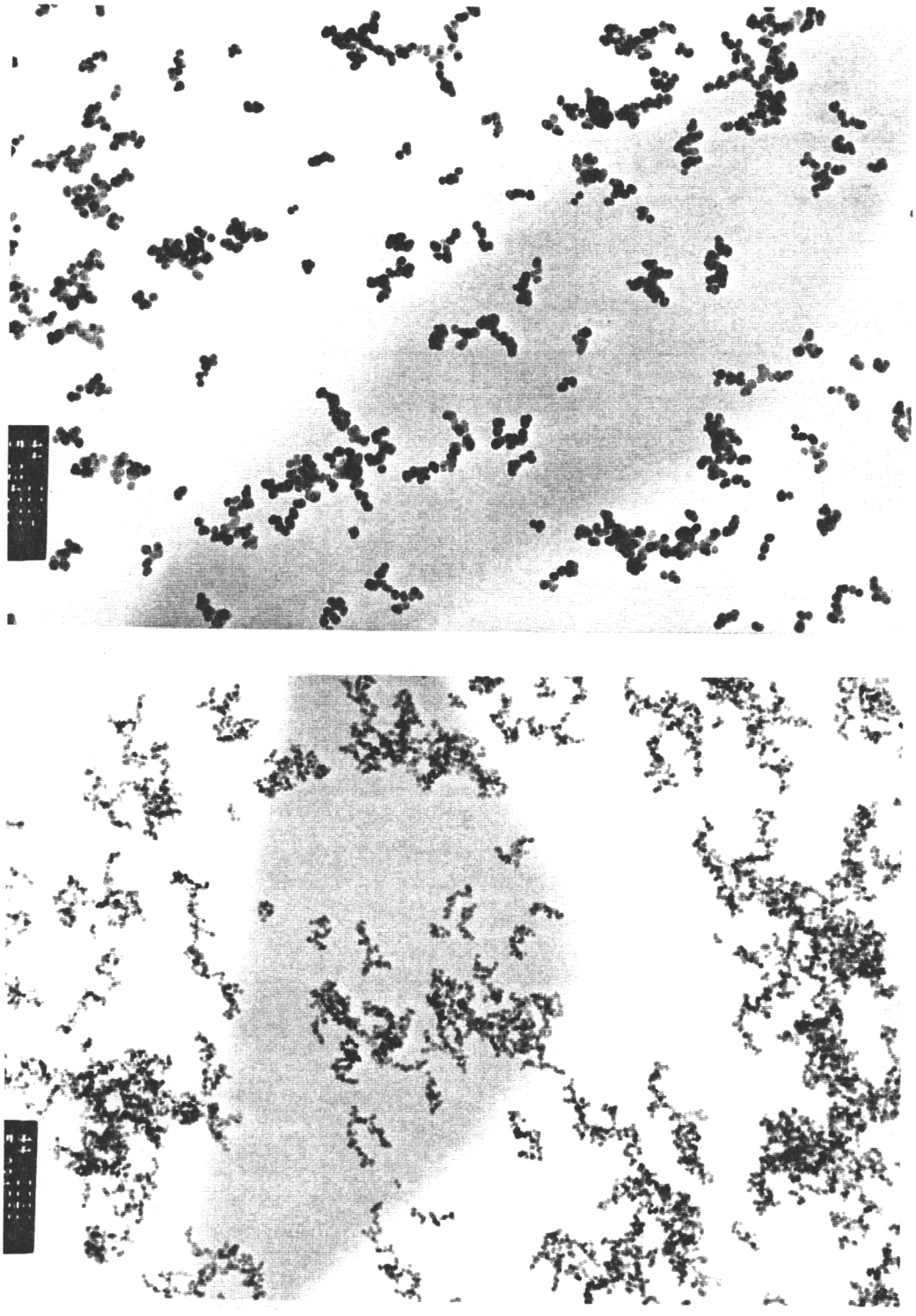

Figure 21. (top) Condition 5, Height = 12.7 mm, No Voltage, $TiCl_4$ 3.2 ml/s, 24K
(bottom) Condition 6, Height = 12.7 mm, No Voltage, $TiCl_4$ 1.6 ml/s, 24K
Scale Bar = 560 nm

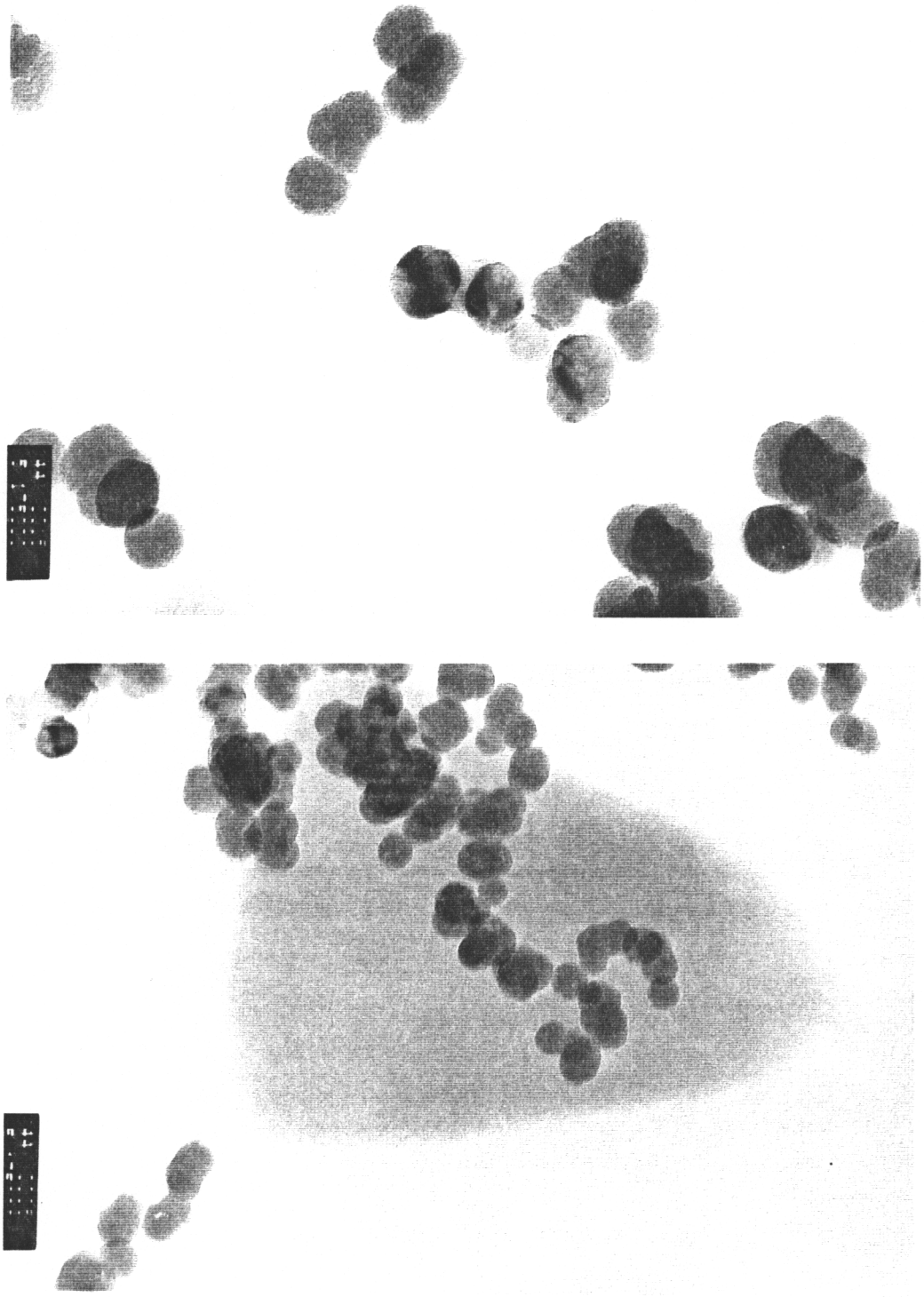

Figure 22. (top) Condition 5, Height = 12.7 mm, No Voltage, $TiCl_4$ 3.2 ml/s, 175K
(bottom) Condition 6, Height = 12.7 mm, No Voltage, $TiCl_4$ 1.6 ml/s, 175K
Scale Bar = 77 nm

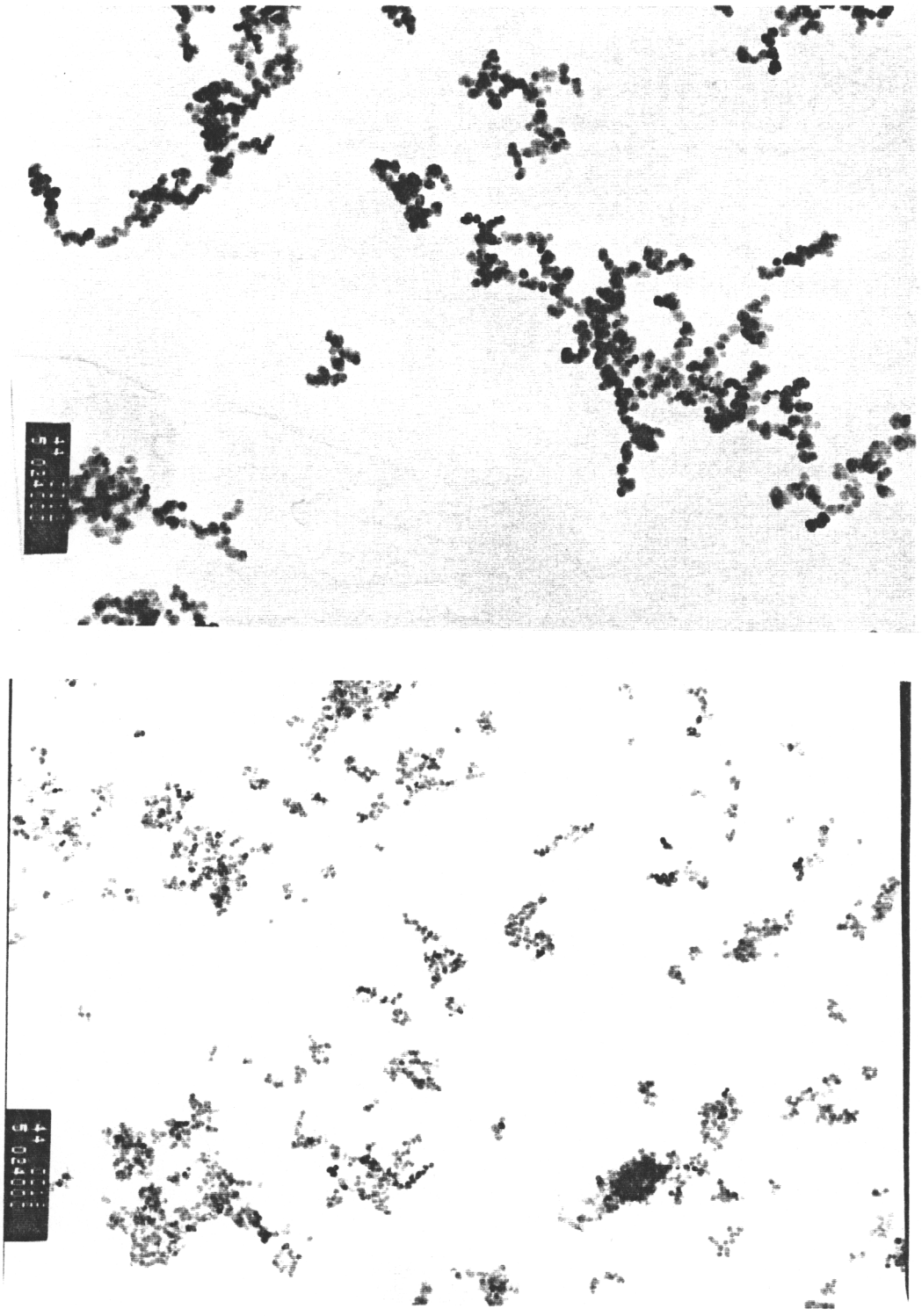

Figure 23. (top) Condition 9, Height = 15.2 mm, No Voltage, $TiCl_4$ 3.2 ml/s, 24K
(bottom) Condition 10, Height = 15.2 mm, No Voltage, $TiCl_4$ 1.6 ml/s, 24K
Scale Bar = 560 nm

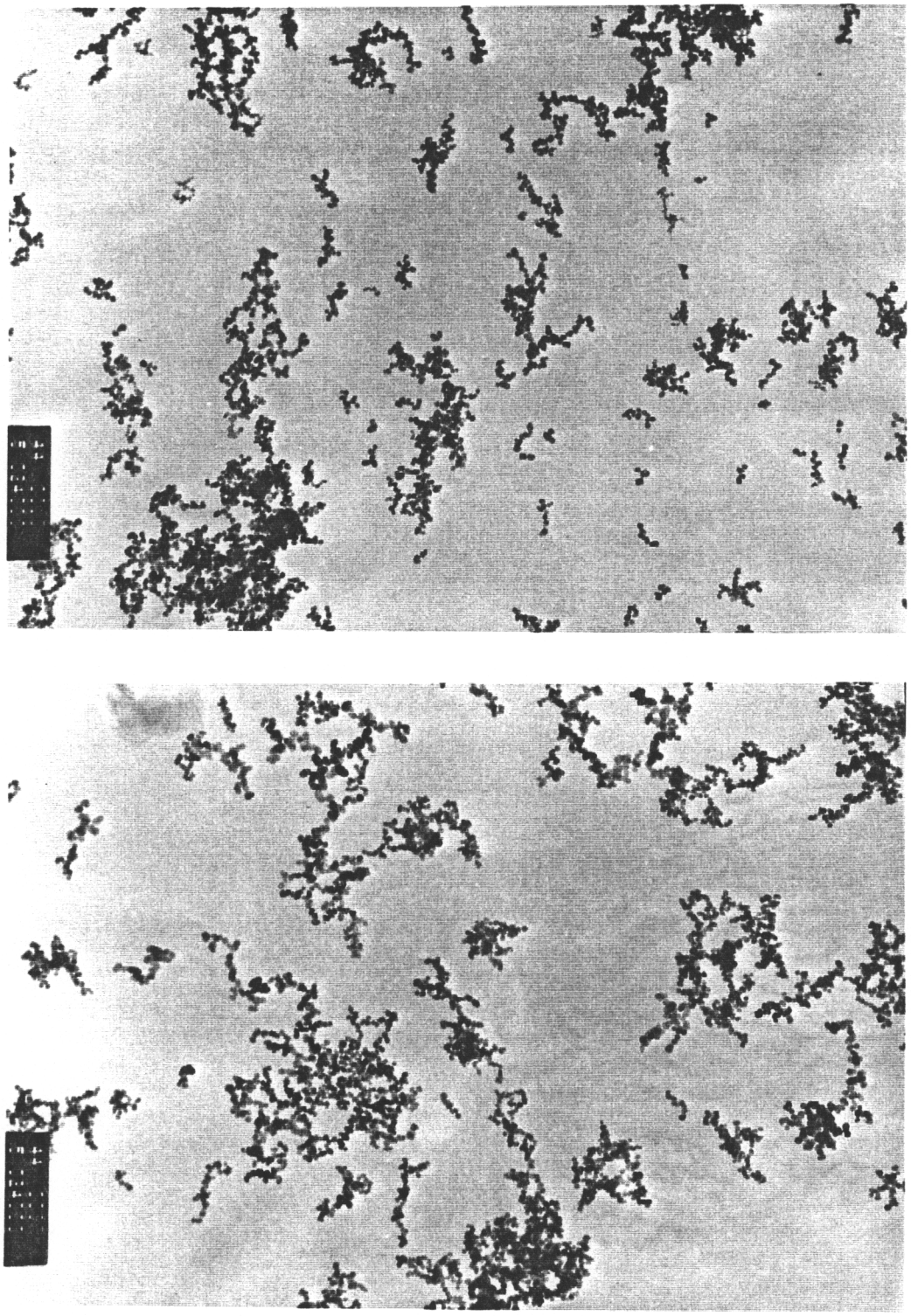

Figure 24. (top) Condition 2, Height = 10.2 mm, No Voltage, $TiCl_4$ 1.6 ml/s, 24K
(bottom) Condition 3, Height = 10.2 mm, -480 Volts, $TiCl_4$ 1.6 ml/s, 24K
Scale Bar = 560 nm

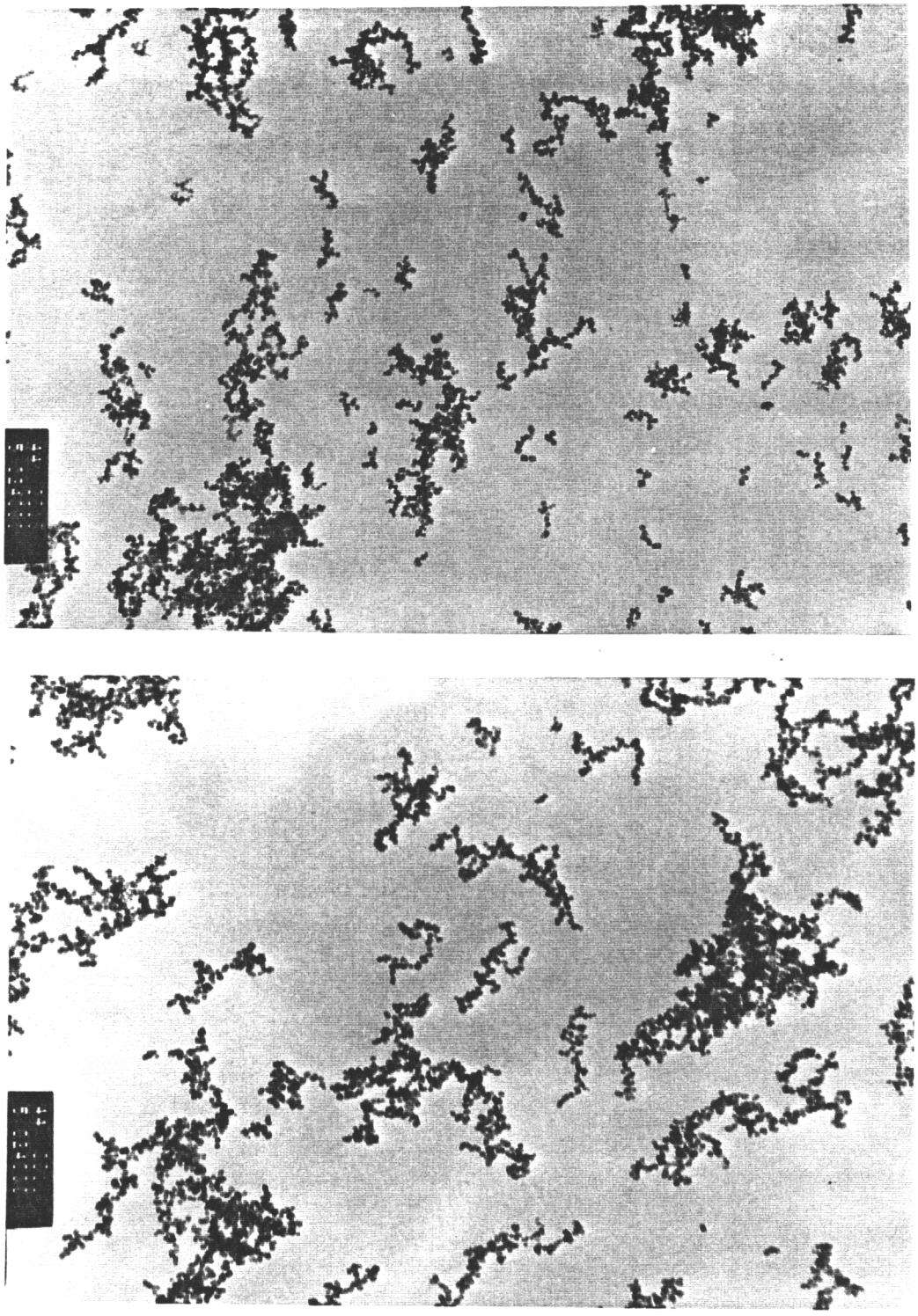

Figure 25. (top) Condition 2, Height = 10.2 mm, No Voltage, $TiCl_4$ 1.6 ml/s, 24K
(bottom) Condition 3, Height = 10.2 mm, -480 Volts, $TiCl_4$ 1.6 ml/s, 24K
Scale Bar = 560 nm

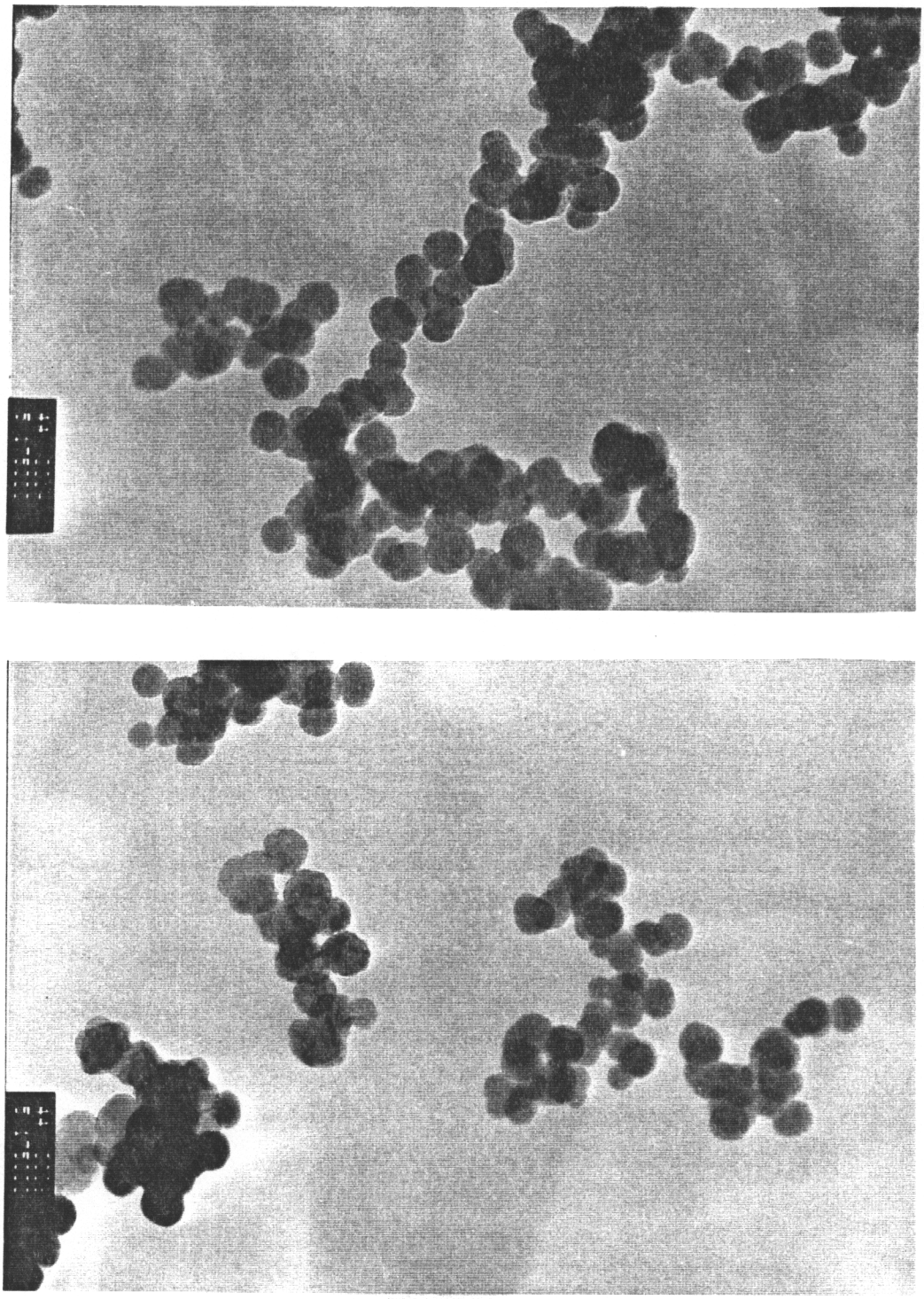

Figure 26. (top) Condition 2, Height = 10.2 mm, No Voltage, $TiCl_4$ 1.6 ml/s, 175K
(bottom) Condition 3, Height = 10.2 mm, -480 Volts, $TiCl_4$ 1.6 ml/s, 175K
Scale Bar = 77 nm

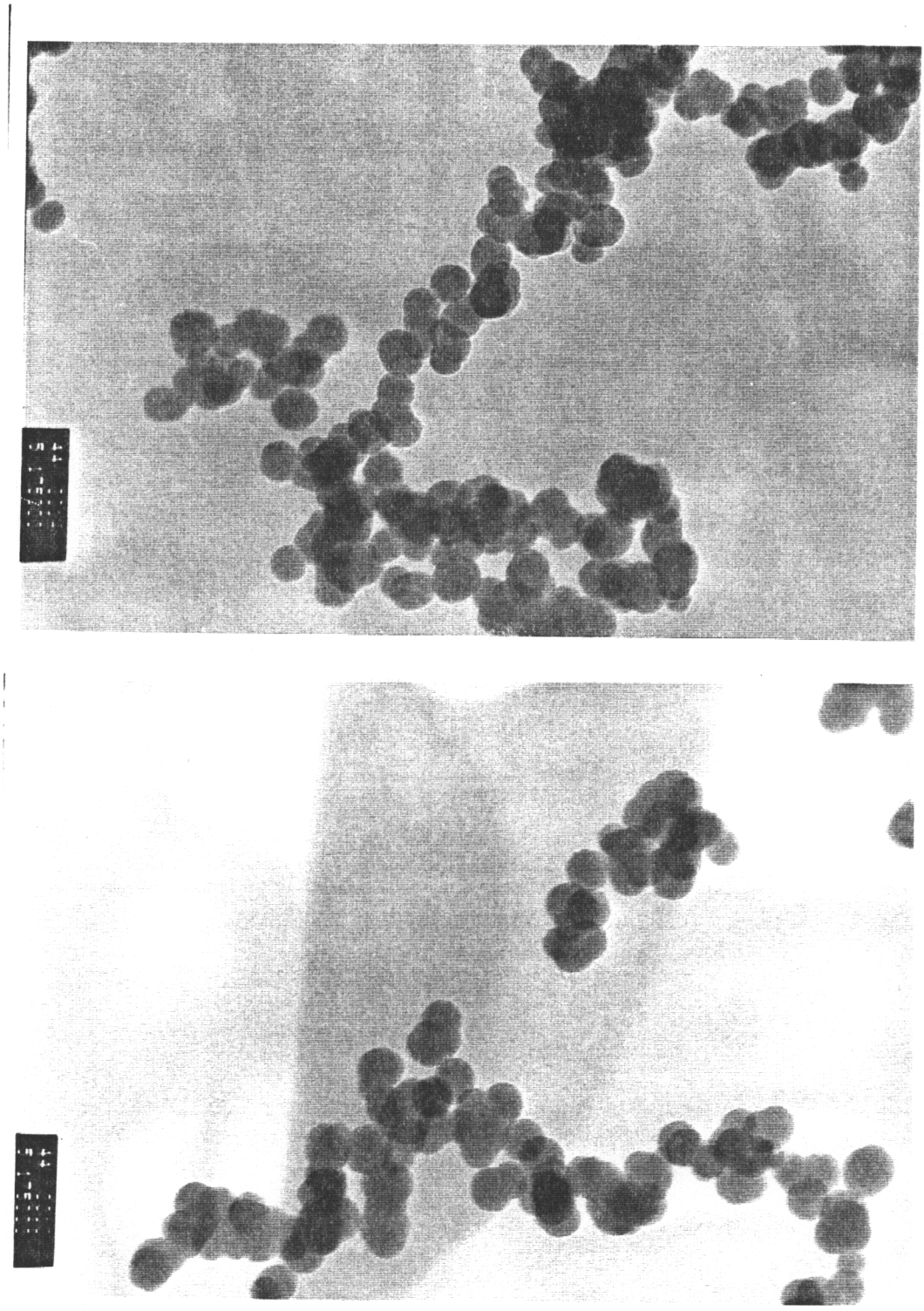

Figure 27. (top) Condition 2, Height = 10.2 mm, No Voltage, $TiCl_4$ 1.6 ml/s, 175 K
(bottom) Condition 4, Height = 10.2 mm, +1040 Volts, $TiCl_4$ 1.6 ml/s, 175K
Scale Bar = 77 nm

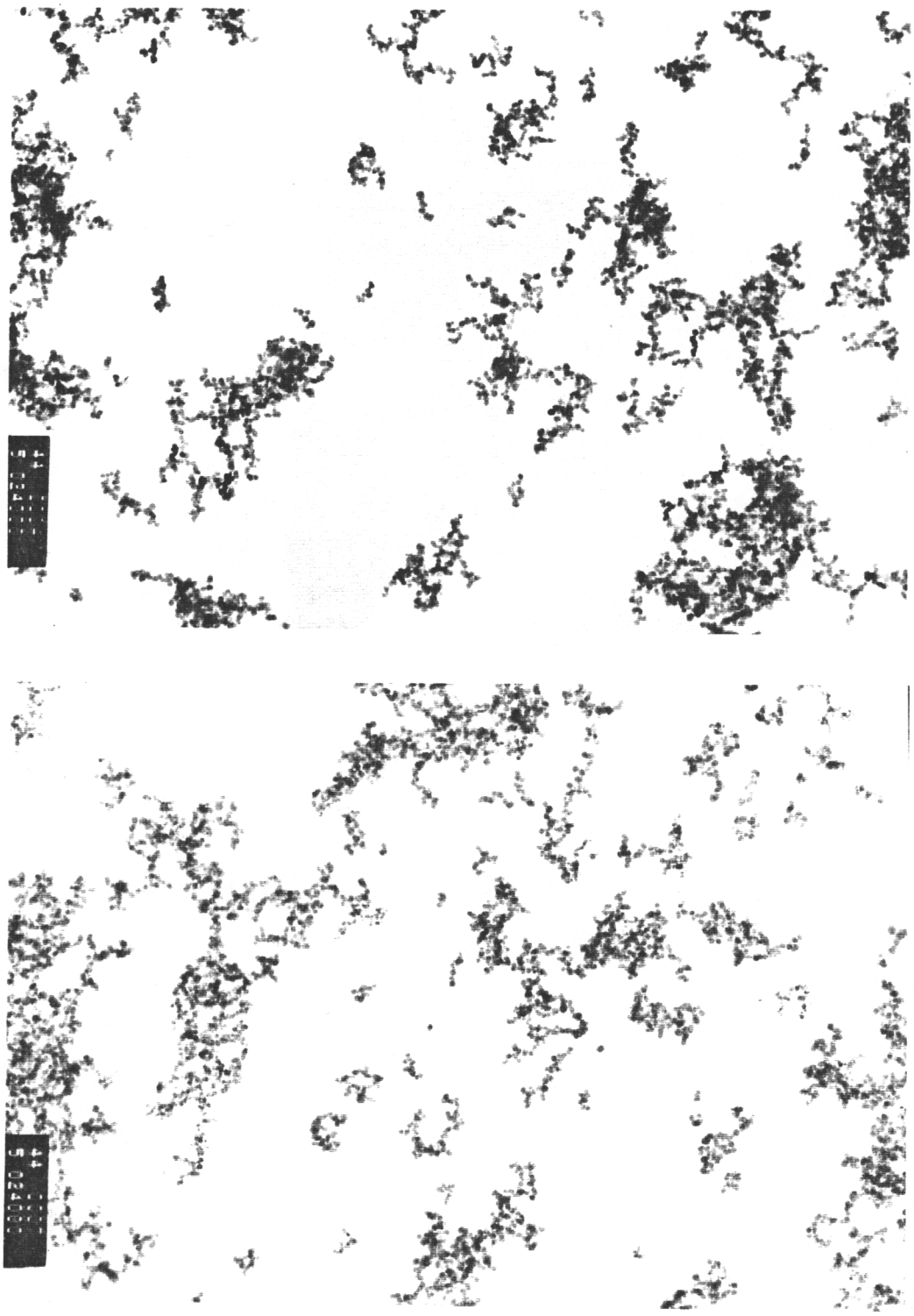

Figure 28. (top) Condition 6, Height = 12.7 mm, No Voltage, $TiCl_4$ 1.6 ml/s, 24K
(bottom) Condition 7, Height = 12.7 mm, -900 Volts, $TiCl_4$ 1.6 ml/s, 24K
Scale Bar = 560 nm

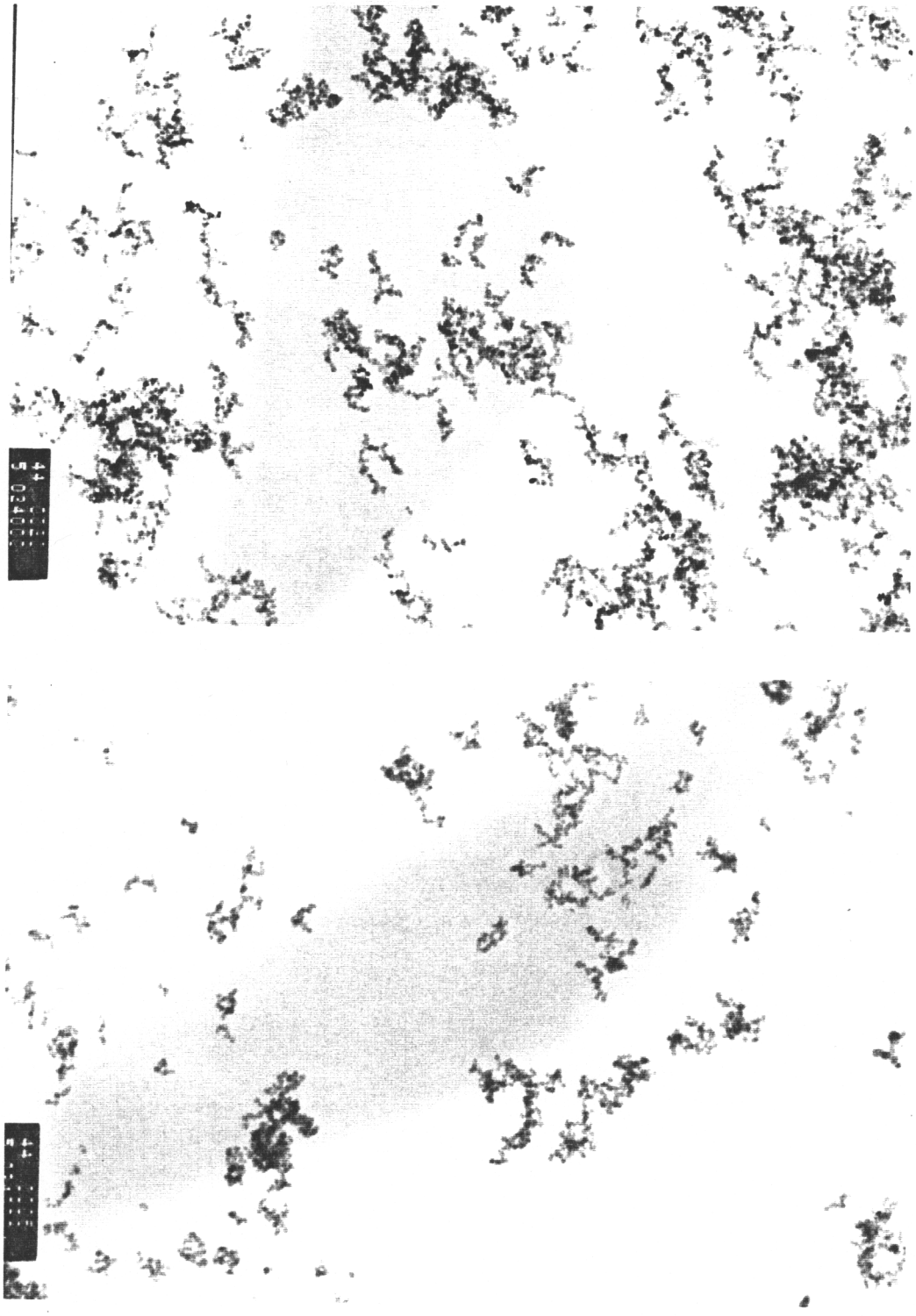

Figure 29. (top) Condition 6, Height = 12.7 mm, No Voltage, $TiCl_4$ 1.6 ml/s, 24K
(bottom) Condition 8, Height = 12.7 mm, +1040 Volts, $TiCl_4$ 1.6 ml/s, 24K
Scale Bar = 560 nm

Even though the resolution of the probe was not sufficient to calculate a growth rate for the particles, it is clear from conditions 1,5,9 and 2,6,10 as well as from the qualitative scattering data that the growth rate is quite rapid. Samples taken below approximately 10 mm failed to collect anything significant, and the effective reaction zone ended at the recirculation zone about 6-7 mm later.

In the TEM photographs, the particles sometimes appear to be very loosely agglomerated in chains and other times seem clumped in groups or layered. There appears to be no correlation between the appearance of the particles layout on the TEM grids and any variable studied. This, of course, does not mean that there is no relationship between the studied variable and the particles, but implies that there is an uncontrolled variable present. Possibilities such as the random (but selective) nature of which areas of the extensive TEM grid were photographed as examples of that condition and the transfer process from the probe onto the TEM grid are most likely responsible. Several shots were taken of every grid, but obviously only a small percentage of the area is represented. It is possible that various areas of one sample might have exhibited different layouts. A comparison between two negatives taken from the same sample, shown in Figure 30, shows that the particle size is equivalent but that the agglomeration is not necessarily the same between two areas on the same grid. The distribution of the particles prior to their attachment to the TEM grid is unknown, but it seems likely that static and surface forces would effect the arrangement of the particles on the grid and that the chains and loose agglomerations might be either broken up or created in the transfer between the probe and the grid. These forces cannot change the size of individual particles thus size trends noted in the data are valid. Any conclusions drawn from the layout of the particles on the negatives would, however, be suspect.

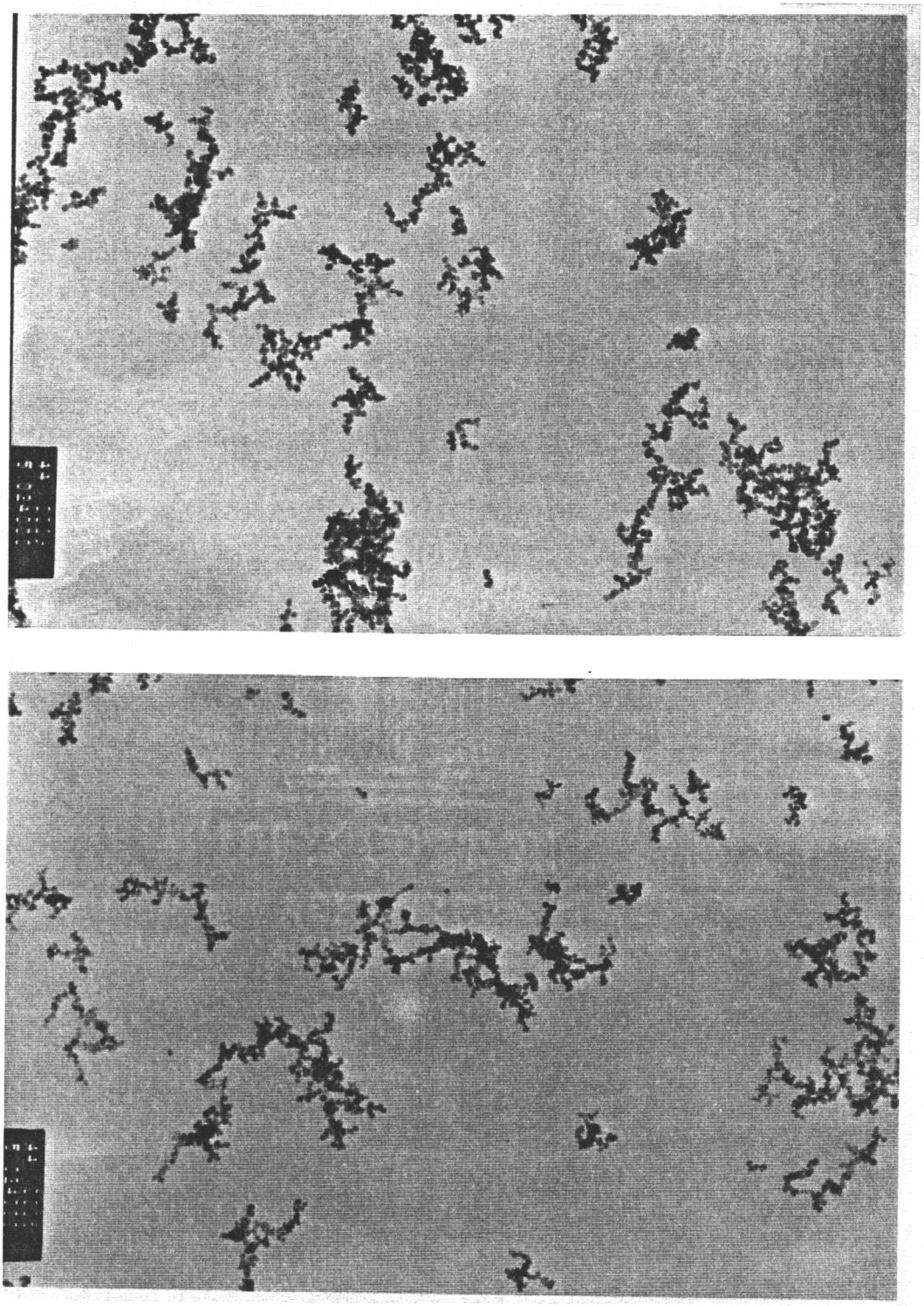

Figure 30. (top) Condition 4, Height = 10.2 mm, +1040 Volts, $TiCl_4$ 1.6 ml/s, 24K
(bottom) Condition 4, Height = 10.2 mm, +1040 Volts, $TiCl_4$ 1.6 ml/s, 24K
Scale Bar = 560 nm

A significant problem with the probe sampling technique was its intrusive effect on the reaction zone. When the probe was placed into the reactor, the reaction zone in the immediate vicinity of the probe did not move or alter significantly with the addition of electric fields. The reaction zone was stabilized on the probe thermally, and therefore no changes in the particles could be observed in the TEM negatives. Decreasing the size of the probe was considered, but practical considerations concerning the transfer of particles between the small probe and the TEM grid presented obstacles that were never fully resolved.

A second explanation for the inconclusive results concerning the application of the electric field may be due to the low concentration of the reactant in the electric field cases. The fact that the development of the size distribution was very quick in these cases may have made any effect due to the electric field undetectable.

In order to obtain better spatial resolution and measure the particles size non-intrusively, *in-situ* optical techniques were attempted.

3.5 Optical Particle Sizing Diagnostics

An optical system was assembled around the reactor which involved two separate optical paths as described in section 2.5. Several challenges were faced in the implementation of this optical system.

The first and most difficult problem was the UV optical path in the system. The complex index of refraction of the TiO_2 particles was taken to be 4.22-*i*0.788 (Ribarsky, 1985) with incident light from an excimer laser operating at 337 nm. The UV beam was split, as discussed in section 2.5, so after each pulse a value of I and I_0 was available. From the physics of the situation, it was expected that even if the intensity of the pulse from the laser varied from pulse to pulse, the ratio of the output from the two photodiodes

would remain a constant. This ratio would then be adjusted to 1.0 when there were no particles in the test section. In practice, this ratio was never constant from one pulse to another. Without pulse to pulse repeatability it was not possible to measure attenuation of the signal when particles were present.

The instrument used to measure the output from the two photodiodes was a boxcar averager. A boxcar averager works by briefly opening an electronic gate a select time delay after being triggered. The output of the boxcar is an integration of how long the gate is open and the magnitude of the input signal. The boxcar can store the acquired signal during the time the gate is open either as a weighted exponential average or by adding it linearly to the previously acquired signal. In order to compare each pulse's I and I_o, the linear mode was chosen, and the boxcar was read and cleared after each pulse.

The timing between the laser pulse, the boxcar averager, and the computer was critical and is most suspect in the inability to get a consistent signal. The most promising configuration was using the computer as the master controller. The computer both triggered the laser and the boxcar averager, then read the output from the boxcar, cleared the boxcar, and repeated the process.

Ideally, the boxcar's gate will open just ahead of the input pulse and close after its completion. However, when watching the oscilloscope traces of the gate and the response of the photodiodes, the symptom of the consistency problem became clearer, but the problem itself remained mysterious. Either the gate or the response pulse from the photodetector did not remain a steady time delay after the trigger, but jumped around. Sometimes the pulse wouldn't even occur within the gate and sometimes it would only be partly in the gate. The end result was that no absorption data was ever collected.

It is also possible that the response of the photodiodes to the laser pulse was inconsistent due to non-linearity in or saturation of the optical material itself. Each pulse

of the excimer laser was expected to have up to 7 mJ of power. The observed response of the electronics on an oscilloscope was well within the limits of the photodiode and amplification circuit, but, since the output is a combination of the photodiode response and the electrical response, the signal viewed on the oscilloscope could have been the electronics' response to a briefly saturated photodetector.

Scattering measurements were also attempted with the setup described in section 2.5. The scattering optics were checked using nitrogen, methane, and propane. With the test section open and no flame, the error was less than 5% compared with the known ratios. When windows were in the test section, light scattering from the glass filled the test section with light noise and made quantitative measurements impossible.

4 Summary and Conclusions

The results of this study can be summarized as:

a) It is possible to consistently generate nanosize ceramic particles in a relatively simple, flame based co-annular reactor.

b) The effect of increasing the ceramic powder's reactant concentration is to increase the average diameter of the final product. This result is consistent with previous researcher's results.

c) The alpha-source charging system in its current design is ineffective at unipolar charging the forming particles.

d) Particles generated within this reactor are affected by an applied electric field.

e) The effect of the applied electric field on the average diameter and size distribution of the ceramic particles was inconclusive.

These conclusions suggest several avenues of continued research.

The first priority in continued research should be to establish a reliable charging system. The primary concern should be to use oxygen or another gas that will allow the formation of ion pairs in the reactant stream. Adachi *et al* (1992) used air in their experiment, implying that 21% oxygen is a sufficient concentration. One possible approach would be to build a charger exactly like the one used by Adachi *et al* (1992). The methodology would be to establish charging in a manner identical to Adachi *et al* (1992) and then modify the design with step-by-step changes into a flow reactor similar to the one used in the present experiments. In order to run these experiments it is necessary to acquire instrumentation capable of estimating the charge density in the reactor. An electrometer capable of reading in the range of nano-amperes to micro-

amperes would allow these measurements. Special cautions, such as neutralizing the reactant stream before it enters the new reactor, should be considered unless it can be proven unnecessary by measurements with the electrometer.

The next priority should be making the optical diagnostics operational to confirm whether or not the particle growth can be controlled by the electric fields. Two obstacles block operation of the system in its current configuration - synchronization of the extinction measurements and light noise in the test section. The synchronization between the laser and extinction signal acquisition equipment must be perfected. This could include additional timing circuits as well as better software control of the process. It is possible that the excimer laser or the boxcar averager will perform better at different repetition rates than those tried so far. To eliminate noise during scattering measurements the test section has been re-designed to lower the amount of laser light that scatters from the windows onto the back of the test section. Tunnels have been built at each window in the test section, as shown in Figure 31, to minimize light noise.

A third recommendation is to consider rebuilding the reactor in such a way as to keep the electric field lines parallel with the streamlines. Even in the Katz & Hung (1990) opposed flow burner, the electric field lines were parallel with one another but the streamlines, with the exception of the stagnation line, were not. A fundamental problem with the current design is its instability. With the flame around the outside of the reaction zone, it is difficult to both keep a controlled flow field and maintain a thermal environment that gives all particles equal time-temperature histories. This configuration also makes retrieval of the particles difficult.

A fourth point of consideration is the design of a system for successfully removing the particles from the reactor without changing their size or size distribution.

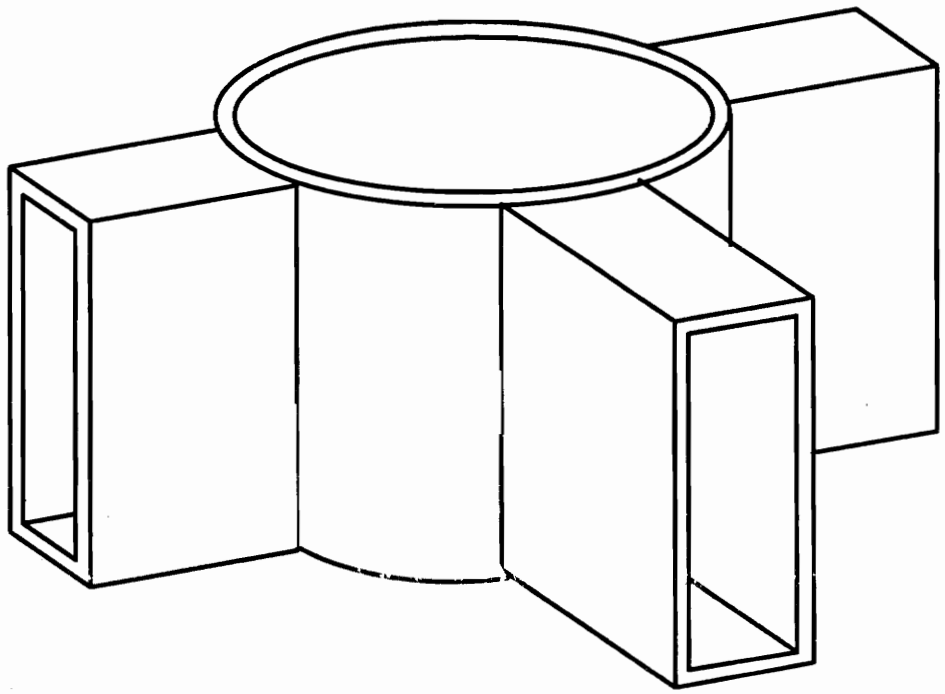

Figure 31. Modified test section with tunnels to minimize light scattered from windows into back of test section.

This would be imperative before the system could be used to produce any significant amount of ceramic powder, either in the laboratory or commercially.

References

Adachi, M., Romay, F. J., Pui, Y. H., "High-Efficiency Unipolar Aerosol Charger Using a Radioactive Alpha Source," *J. Aerosol Science*, Vol. 23, No. 2, 123-137, 1992.

Beckwith, T. G., Marangoni, R. D., *Mechanical Measurements* (4th ed), Addison-Wesley Publishing Company, 1990.

Bohren, C. F., Huffman, D. R., *Absorption and Scattering of Light by Small Particles*, John Wiley and Sons, 1983.

Brown, A. S., "Ceramics learn to bend instead of break," *Aerospace America*, 24-28, Aug. 1990.

Davis, R. M., Department of Chemical Engineering, Virginia Polytechnic Institute and State University, private communications, 1994.

Flagan, R. C., "Aerosol Routes for Powder Synthesis," *Ceramic Powder Science II*, Vol 1., The American Ceramic Society, 229-242, 1988.

Hardesty, D. R., Weinberg, F. J., "Electrical Control of Particulate Pollutants From Flames," Fourteenth Symposium (International) on Combustion, 907-918, 1972.

Hidy, G. M., Brock, J. R., *The Dynamics of Aerocolloidal systems*, Pergamon Press, 296-305, 1970.

Johnson, D. W., Jr., "Innovation in Ceramic Powder Preparation," *Advances in Ceramics, vol. 21: Ceramic Powder Science*, 3-19, The American Ceramic Society, 1987.

Katz, J. L., Hung, C., "Initial Studies of Electric Field Effects on Ceramic Powder Formation in Flames," Twenty-Third Symposium (International) on Combustion, The Combustion Institute, 1733-1738, 1990.

Kent, J. H., "A Noncatalytic Coating for Platinum-Rhodium Thermocouples," *Combustion and Flame*, **14**, 279-281, 1970.

Kerker, M., *The Scattering of Light and Other Electromagnetic Radiation*, Academic Press, 1969.

Lawton, J., Weinberg, F. J., *Electrical Aspects of Combustion*, Clarendon Press, 1969.

(a) Pratsinis, S. E., Bai, H., Biswas, P., Frenklach, M., Mastrangelo, S. V. R., "Kinetics of Titanium(IV) Chloride Oxidation," *J. Am. Ceram. Soc.*, **73**, 2158-62, 1990.

(b) Pratsinis, S. E., Landgrebe, J. D., Mastrangelo, S. V. R., "Design Correlations for Gas Phase Manufacture of Ceramic Powders," *J. Aerosol Science*, Vol. 20, No. 8, 1457-1460, 1989.

Ribarsky, M. W., *Handbook of Optical Constants of Solids*, Academic Press, 795-804, 1985.

Santoro, R. J., Semerjian, H. G., Dobbins, R. A., "Interpretation of Optical Measurements of Soot in Flames," AIAA 18th Thermophysics Conference, AIAA-83-1516, 1983.

Sanzone, G., Department of Chemistry, Virginia Polytechnic Institute and State University, private communication, 1994.

Shackelford, J. F., *Introduction to Materials Science for Engineers*, Macmillian Publishing Company, 275-279, 1988.

Wu, J. J., Nguyen, H. V., Flagan, R. C., "A Method for the Synthesis of Submicron Particles," *Langmuir*, **3**, 266-71, 1987.

Zachariah, M. R., Chin, D., Semerjian, H. G., Katz, J. L., "Silica Particle Synthesis in a Counterflow Diffusion Flame Reactor," *Combustion and Flame*, 78: 287-298, 1989.

Appendix A Optical Measurement of Small Particles

A.1 Light Scattering and Absorption by Small Particles

Lord Rayleigh's original derivation of light scattering from very small particles compared with the incident wavelength was based on reasoning and the dimensions of the variables involved in the problem (reproduced in Bohren & Huffman, 1983). This correctly describes the $1/\lambda^4$ light scattering relationship. This approximation, known as the electrostatic approximation, is electromagnetically based on the fact that, when a particle is small compared with the wavelength, the instantaneous field experienced by the particle is virtually uniform across the particle. The electric field around the particle is then the field caused by an electric dipole. Solution of the field equations significantly far from the particle leads to a relatively simple algebraic relationship between the scattering and extinction of light by a sphere and the sphere's diameter. In 1908, Gustav Mie applied Maxwell's equations to a suspension of gold particles in water. This exact solution to the light scattering from a sphere, known as Mie theory, reduces to the electrostatic case when particles are small compared to the wavelength, generally considered when the diameter of the particle is less than one tenth the incident wavelength. This is the nominal limit for the Rayleigh regime.

The following is a description of the method used to determine particle diameter from light scattering and absorption data using Rayleigh theory. The basic derivation of these equations, having been done many times before by others, has been excluded. The following explanations are based on derivations found in the texts of Kerker (1969) and Bohren & Huffman (1983).

The solution to the electrostatic problem is often expressed in terms of cross sections. The scattering cross section is given by:

$$C_{sca} = \frac{2\pi^5 d^6}{3\lambda^4}\left|\frac{m^2-1}{m^2+2}\right|^2$$

where C_{sca} is the total energy scattered by a particle in all directions and d is the diameter, $\lambda$is the wavelength, and m is the particle's complex index of refraction. The commonly quoted efficiency factor for scattering is found by dividing this by the actual geometric cross section of the particle, $\pi d^2/4$. This quantity,

$$Q_{sca} = \frac{8\pi^4 d^4}{3\lambda^4}\left|\frac{m^2-1}{m^2+2}\right|^2$$

represents the fraction of energy geometrically incident upon the particle which is scattered in all directions.

The scattering coefficient is commonly used when sizing many particles in a suspension since it is related to both the size of the particles and the number of particles. This quantity, also called the volumetric scattering cross section or the Rayleigh ratio, is

$$Q_{ij} = NC_{ij}$$

where Q_{ij} is the energy scattered by a unit volume in the direction θ, per steradian, with a linearly polarized incident beam of unit intensity and N being the number density of the particles. The quantity Q_{ii}, by calibrating against gases of known cross section C_{ii} and number density, can be measured experimentally. The differential scattering cross section, C_{ij}, is the energy scattered by a particle in the direction θ, per steradian, with a linearly polarized incident beam of unit intensity. The subscripts i and j represent the state of polarization of the scattered and incident light respectively. The letters v and h are used to designate vertical (perpendicular to the scattering plane) and horizontal (parallel to the scattering plane) polarization. The differential scattering cross sections are given by Rayleigh theory to be

$$C_{vv} = \frac{\pi^4 d^6}{4\lambda^4}\left|\frac{m^2-1}{m^2+2}\right|^2 \qquad \text{and}$$

$$C_{hh} = \frac{\pi^4 d^6}{4\lambda^4}\left|\frac{m^2-1}{m^2+2}\right|^2 \cos^2\theta$$

In an experiment with the incident light vertically polarized, all light scattered in the scattering plane will be independent of the scattering angle. It is easily seen that scattering data alone does not yield direct information about the diameter since the measured intensity is directly proportional to the particle number density, another unknown.

As light travels through a test section of small particles, its energy is reduced by both scattering and absorption. Extinction is the quantity measured by a detector, and is the sum of these two effects. The relation

$$\frac{I}{I_o} = \exp(-K_{ext} l)$$

describes the attenuation of light as it travels a distance l through a particle suspension with extinction coefficient K_{ext}. The term I_o is the intensity of light passing through the surrounding medium when no particles are present. The extinction coefficient is given by

$$K_{ext} = NC_{ext}$$

and

$$C_{ext} \cong \frac{\pi^2 d^3}{\lambda}\mathrm{Im}\left(\frac{m^2-1}{m^2+2}\right)$$

where the approximate extinction cross section C_{ext} is, as defined by electrostatic theory, accurate only when the scattering contribution towards extinction is small compared with absorption. This is generally true in the Rayleigh regime, but if the condition $|m|x << 1$ where $x=\pi d/\lambda$ is not satisfied, errors may result.

When both the values of Q_{vv} and K_{ext} are determined by experimental measurements and the complex index of refraction is assumed to be known at the given wavelength, enough information is available to solve directly for the particle diameter.

$$\frac{Q_{vv}}{K_{ext}} = \frac{NC_{vv}}{NC_{ext}} = \frac{\frac{\pi^4 d^6}{4\lambda^4}\left|\frac{m^2-1}{m^2+2}\right|^2}{\frac{\pi^2 d^3}{\lambda}\mathrm{Im}\left(\frac{m^2-1}{m^2+2}\right)}$$

Dividing these two quantities eliminates N as a variable. Simplifying and rearranging to solve for d this becomes

$$d = \left[\frac{4\lambda^3 Q_{vv}}{\pi^2 K_{ext}} \frac{\mathrm{Im}\left(\frac{m^2-1}{m^2+2}\right)}{\left|\frac{m^2-1}{m^2+2}\right|^2}\right]^{\frac{1}{3}}$$

where d is the diameter in a monodisperse particle field.

If scattering and absorption are occurring at different wavelengths, then the relationship between Q_{vv}, K_{ext}, and d becomes

$$d = \left[\frac{4Q_{vv}}{\pi^2 K_{ext}} \frac{\lambda_s^4}{\lambda_a} \frac{\mathrm{Im}\left(\frac{m^2-1}{m^2+2}\right)}{\left|\frac{m^2-1}{m^2+2}\right|^2}\right]^{\frac{1}{3}}$$

where λ_s is the wavelength where Q_{vv} is being measured and λ_a is the wavelength where K_{ext} is being measured.

Even though Rayleigh theory does not yield any information about the size distribution, this quantity can be approximated by assuming a size distribution and width as shown by Santoro, Semerjian, & Dobbins (1983). In that paper the properties of C_{vv} and C_{ext} are calculated as functions of a log-normal size distribution with an assumed standard deviation. A program for reducing optical data using this method is supplied on the following pages. Measurement of the size distribution requires additional observations and the use of the Mie theory.

A.2 Program for the Calculation of Average Particle Diameter

```
      PROGRAM RAYLEIGH
      IMPLICIT REAL(A-Z)
      INTEGER I,J,K
      COMPLEX M,MM
      COMMON /PD/D,Dg,Og

      OPEN(UNIT=61,FILE='OPDAT.DAT',STATUS='OLD')

      PI=3.141593

C     File OPDAT.DAT contains data in the following order:
C     index of ref (real)      ind of ref (img)
C     Qvv of unknown, Kext of unknown
C     Wavelength absorb (nm)   Wavelength scatter (nm)
C     assumed geometric mean standard deviation

      READ(61,*)M
      READ(61,*)QVV,KEXT
      READ(61,*)ALMBDA,SLMBDA
      READ(61,*)Og

      FN=EXP(9.0*Og**2.0)
      WRITE(*,*)
      WRITE(*,'(1X,"Rayleigh calculation with Og = ",F7.3)')Og
      WRITE(*,'(1X,"       ( calculation with fn = ",F7.3," )")')FN
      WRITE(*,*)


C     Guessed value of geometric mean diameter (nm)
      Dg=30.0


      MM=(M**2.0-1.0)/(M**2.0+2.0)

      FM=(ABS(MM))**2.0
      EM=AIMAG(MM)
      LAMR=(SLMBDA**4.0)/ALMBDA
```

```
30  CALL MOM(6.0,3.0,D63)
    STOR=Dg
    Dg=Dg-Dg/400.0
    CALL MOM(6.0,3.0,DD63)
    Dg=STOR

    KONS=(4.0*PI*EM*QVV*LAMR/(KEXT*PI**2.0))**(1.0/3.0)

    F=D63-KONS
    DEL=(D63-DD63)/(Dg/400.0)
    DO=Dg
    Dg=DO-.8*F/DEL
    DDg=ABS(Dg-DO)/Dg
    IF (DDg.GT.0.001) GOTO 30

    N=LAMBDA*KEXT*FN/(EM*D63**3.0*PI**2.0)
    WRITE(*,*)Dg,N
    END

    SUBROUTINE MOM(P,Q,DPQ)
    IMPLICIT REAL(A-Z)
    INTEGER I,J,K
    COMMON /PD/D,Dg,Og

C   Statement function of logarithmic probability distribution
    PD(D,Dg,Og)=EXP(-(LOG(D/Dg)/(1.414214*Og))**2.0)/(2.50663*Og*D)

    DD=Dg/20.0
    D=0.0
    IN1=0.0
    IN2=0.0

10  CONTINUE
    D=D+DD/3.0
    IN1=IN1+PD(D,Dg,Og)*D**P*DD
    IN2=IN2+PD(D,Dg,Og)*D**Q*DD
    IF (D.LT.20.0*Dg) GOTO 10
    DPQ=(IN1/IN2)**(1/(P-Q))
    RETURN

    END
```

Appendix B Error Analysis

B.1 Analysis Methods

An analysis of the error expected from measurement of the particle size both by counting and by optical methods was conducted. In the case of the optical analysis, no numbers are available since no optical data was collected.

B.2 TEM Particle Size Analysis

In order to quantify the size and standard deviation of the particles photographed by the TEM, a counting method was used. For negatives taken at 175 K magnification, a random sample of 30 particles from each negative were counted and placed into 5 nm groups, as Table B.1 demonstrates. For negatives taken at 24 K magnification, a sample of 50 particles was taken, but because the particles appeared smaller on the negative, they were counted into 10 nm groups, as shown in Table B.2.

Because the number of particles in the total population is much greater than 30 or 50, a sample distribution was used to perform the statistical average. The average particle diameter, based on the analysis in Beckwith & Maringoni (1990), is:

$$\bar{d} = \sum_{i=1}^{n} \frac{d_i}{n} = \frac{d_1 + d_2 + \ldots + d_n}{n}$$

and one standard deviation, S, is:

$$S = \sqrt{\frac{\sum_{i=1}^{n} (d_i - \bar{d})^2}{n-1}} = \sqrt{\frac{\sum_{i=1}^{n} \Delta d^2}{n-1}}.$$

The specific particle diameters are taken as the midpoints of the individual groupings.

Sample Calculation:

175K Magnification of Condition 6

Particle Diameter, d	Number of Results, n	Deviation, Δd	Δd^2
12.5	2	-9.00	81.00
17.5	10	-4.00	16.00
22.5	10	1.00	1.00
27.5	8	6.00	36.00
$\sum d = 645$	$\sum n = 30$		$\sum \Delta d^2 = 620$

$$\bar{d} = \frac{645}{30} = 21.5$$

$$S = \sqrt{\frac{620}{29}} = 4.62$$

Table B.1. Samples from 175 K Magnification:

	Particle Diameters (nm)								Statistical Analysis (nm)	
CASE	10-15	15-20	20-25	25-30	30-35	35-40	40-45	45-50	$\overline{d}$	S
2	2	10	16	2					20.50	3.62
3	3	13	12	1	1				19.83	4.30
4	2	4	14	10					22.83	4.34
5				2	3	14	9	2	38.50	4.81
6	2	10	10	8					21.5	4.62

Table B.2. Samples from 24 K Magnification:

	Particle Diameters (nm)						Statistical Analysis (nm)	
CASE	0-11	11-22	22-33	33-44	44-55	55-66	$\overline{d}$	S
1	8	28	14				17.82	7.25
2	6	22	19	3			20.68	8.58
3	2	27	17	4			21.56	7.77
4	3	21	25	1			21.78	7.11
5			3	26	20	1	42.68	6.99
6	1	38	10	1			18.92	5.57
7	7	33	10				17.16	6.45
8	6	29	15				18.48	6.92
9			1	15	28	6	47.08	7.47
10		36	14				19.58	4.99

B.3 Optical Particle Size Determination

What follows is an analysis of the error propagation from measured quantities in the calculation of the diameter of a particle using the equations in section A.1, a monodisperse size distribution. Only the measured values will be considered to propagate error as the other values have been assumed.

The equation for the diameter of a sphere, from A.1, is

$$d = \left[\frac{4Q_{vv}}{\pi^2 K_{ext}} \frac{\lambda_s^4}{\lambda_a} \frac{\mathrm{Im}\left(\frac{m^2-1}{m^2+2}\right)}{\left|\frac{m^2-1}{m^2+2}\right|^2} \right]^{\frac{1}{3}}$$

where the only measured quantities are Q_{vv} and K_{ext}. Rewriting, this becomes

$$d = \left[W \frac{Q_{vv}}{K_{ext}} \right]^{\frac{1}{3}}$$

where W is a constant replacing all the assumed values. The variance of d is

$$\sigma_d^2 = \left(\frac{\partial d}{\partial Q_{vv}} \right)^2 \left(\sigma_{Q_{vv}}\right)^2 + \left(\frac{\partial d}{\partial K_{ext}} \right)^2 \left(\sigma_{K_{ext}}\right)^2$$

where $\sigma_{Q_{vv}}$ and $\sigma_{K_{ext}}$ are the variance of Q_{vv} and K_{ext} respectively. With

$$\frac{\partial d}{\partial Q_{vv}} = -\tfrac{1}{3} W^{\frac{1}{3}} K_{ext}^{-\frac{1}{3}} Q_{vv}^{-\frac{2}{3}}$$

and

$$\frac{\partial d}{\partial K_{ext}} = -\tfrac{1}{3} W^{\frac{1}{3}} Q_{vv}^{\frac{1}{3}} K_{ext}^{-\frac{4}{3}}$$

the variance of d becomes

$$\sigma_d^2 = \tfrac{1}{9} W^{\frac{2}{3}} K_{ext}^{-\frac{2}{3}} Q_{vv}^{-\frac{4}{3}} \sigma_{Q_{vv}}^2 + \tfrac{1}{9} W^{\frac{2}{3}} Q_{vv}^{\frac{2}{3}} K_{ext}^{-\frac{8}{3}} \sigma_{K_{ext}}^2 \quad .$$

The variance is commonly divided by the diameter squared, which leaves

$$\frac{\sigma_d^2}{d^2} = \frac{1}{9}\left(\frac{\sigma_{Q_{vv}}}{Q_{vv}} \right)^2 + \frac{1}{9}\left(\frac{\sigma_{K_{ext}}}{K_{ext}} \right)^2 .$$

Vita

Stephen Damian LePera was born on March 23, 1969 in Harrisonburg Virginia. He lived there until his graduation from Harrisonburg High School in 1987.

Stephen then traveled to Blacksburg, Virginia and began his studies at Virginia Polytechnic Institute and State University. After completing his bachelors degree in Mechanical Engineering, he realized that his career goals would require continued education, and upon acceptance to the graduate school at VPI & SU, stayed in Blacksburg to obtain his master's degree.